Anomalous Electromagnetic Response in the Spin-Triplet Superconductor UTe_2

Unconventional superconductivity with a spin-triplet pairing state has attracted considerable interest because of its unusual nontrivial superconducting order parameters and magnetic response, which are quite different from those of conventional Bardeen-Cooper-Schrieffer superconductors. In particular, the spin-triplet pairing state protected by a topological invariant provides a good opportunity to seek exotic quasiparticles such as Majorana fermions. The recent discovery of unconventional superconductivity in UTe_2 has provided a new opportunity in the research of spin-triplet pairing states in solid state physics [1]. One of the most important challenges for studying the superconducting state of UTe_2 is to clarify its thermodynamic behavior and its magnetic response.

In this study [2], to further understand the spin-triplet superconductivity in UTe_2 from a thermodynamic point of view, we investigate the magnetic field and the temperature dependence of dc magnetization, heat capacity down to 80 mK in magnetic fields up to 14 T. Our high-resolution magnetization measurements done by the Faraday magnetometer for $H \parallel a$ (the magnetic easy axis, Fig. 1(a) and (c)) and for $H \parallel b$ (hard axis, Fig. 1(b) and (d)) reveal multiple

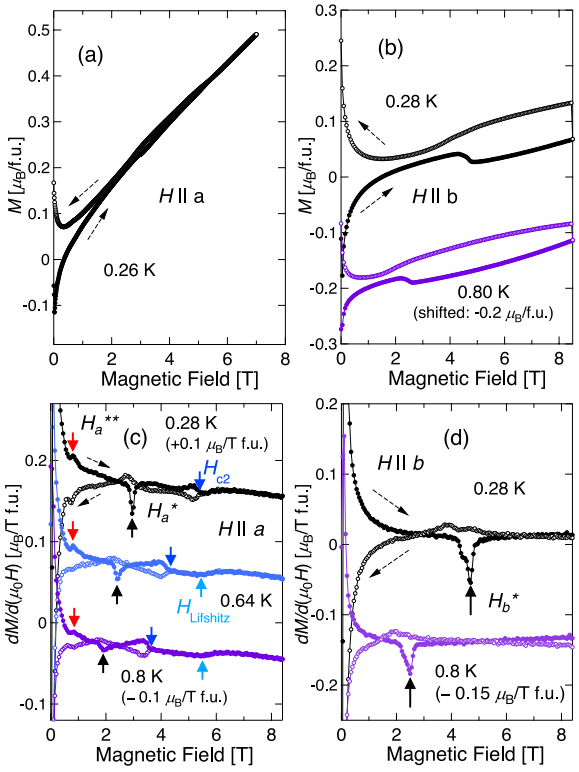

Fig. 1. (a,b) Magnetization curves $M(H)$ of UTe_2 in $H \parallel a$ (a) and in $H \parallel b$ (b). (c,d) The differential of magnetization curves dM/dH in $H \parallel a$ (c) and in $H \parallel b$ (d). The dashed arrows indicate the field sweep direction.

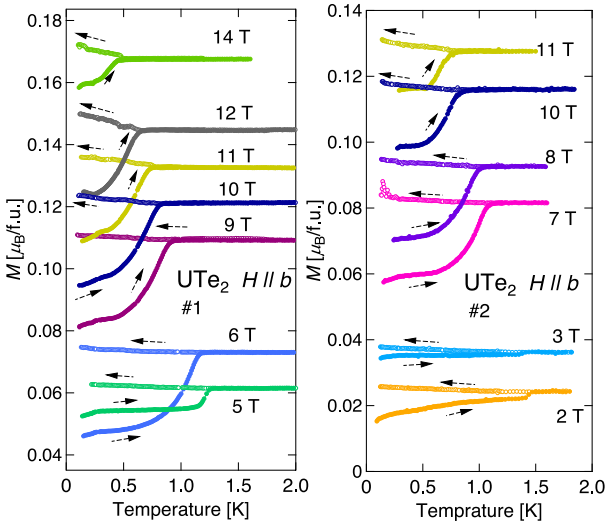

Fig. 2. Temperature dependence of magnetization $M(T)$ at different magnetic fields applied along the b axis of UTe_2 sample #1 (left) and #2 (right). The solid and the open symbols show the data obtained in the warming up process after zero-field cooling and that obtained in subsequent cooling process, respectively.

anomalies (H_a^{**}, H_a^*, and H_b^*) in the field dependence of the magnetization $M(H)$ below the upper critical field (H_{c2}). These anomalies are also observed in our ac susceptibility measurements done down to 30 mK [2].

We further find the temperature dependence of the magnetization, $M(T)$, is changed at the anomaly. Figure 2 shows $M(T)$ observed in two different crystals at different magnetic fields applied along the b axis. As shown in Fig. 2, the difference between zero-field cooling and field-cooling processes in the superconducting state below H_b^* becomes smaller as approaching H_b^* and then larger with strong irreversibility above H_b^*.

These anomalies observed both in $M(H)$ and $M(T)$ in the superconducting phase are attributed to strong pinning effects on vortices in the spin-triplet superconducting state of UTe_2. In addition, we find a broad steplike anomaly just above H_{c2} for the magnetic easy axis ($H \parallel a$). Given that this anomaly does not depend on the temperature and is observed above the superconducting transition temperature, we suggest that this is caused by the Lifshitz transition of this compound.

The anomalous vortex states in UTe_2 suggested by our magnetization measurements are also consistent with recent NMR measurements [3] showing gradual decrease of the NMR Knight shift and shoulder-like anomalies in the NMR spectra. These anomalies observed for 6–10 T indicate the presence of inhomogeneous internal fields, which could be brought by a gradual change of the d-vector of the spin-triplet state in vortices. We suggest that depinning of the d-vector above H_b^* that is pinned to $d \parallel H$ at lower fields might be related to these anomalies observed in our magnetization and the NMR measurements.

References
[1] D. Aoki, K. Ishida, and J. Flouquet, J. Phys. Soc. Jpn. **88**, 022001 (2019).
[2] Y. Shimizu, S. Kittaka, Y. Kono, T. Sakakibara, K. Machida, A. Nakamura, D. Li, Y. Homma, Y. J. Sato, A. Miyake, M. Yamashita, and D. Aoki, Phys. Rev. B **106**, 214525 (2022).
[3] G. Nakamine, K. Kinjo, S. Kitagawa, K. Ishida, Y. Tokunaga, H. Sakai, S. Kambe, A. Nakamura, Y. Shimizu, Y. Homma, D. X. Li, F. Honda, and D. Aoki, J. Phys. Soc. Jpn. **90**, 064709 (2021).

Authors
Y. Shimizu[a], S. Kittaka[b], Y. Kono[b], T. Sakakibara, K. Machida[c], A. Nakamura[a], D. Li[a], Y. Homma[a], Y. J. Sato[a], A. Miyake, M. Yamashita, and Dai Aoki[a]
[a]Institute for Materials Research (IMR), Tohoku University
[b]Chuo University
[c]Ritsumeikan University

PI of Joint-use project: Y. Shimizu
Host lab: Yamashita Group

Theory of Energy Splitting of Chiral Phonons

Chirality is a property manifesting that the system's structure cannot overlap with its mirror image by using any combination of translation and rotation alone, and chiral materials exhibit many interesting cross correlations in their electromagnetic and/or thermal properties. This is due to the property that polar-vector inputs can induce axial-vector outputs and *vice versa* in those systems in addition to ordinary responses, and this cross-correlated response is governed by a "order parameter" represented by an electric toroidal multipole of some rank [1]. Many of the preceding studies on the chiral systems have focused on their electronic properties, since the cross correlated electromagnetic responses are mainly governed by those degrees of freedom.

We have conducted a project to theoretically investigate the effects of chiral structure on phonon properties with mainly targeting tellurium and its related systems [2]. It has been known that these systems have a special quantum number related to their chirality, and it is crystal angular momentum (CAM) m. The main issue is how to characterize an energy splitting of chiral phonons with different CAM values ($m = \pm 1$). Chiral phonons have an elliptic polarization of atomic displacement that rotates clockwise or anticlockwise depending on the sign of CAM m.

For studying this problem, we have first performed a model building within the harmonic approximation for the lattice deformation energy and constructed a related dynamical matrix, the eigenvalues of which determine phonon energies. We have found an important constraint for the dynamical matrix that guarantees the stability of the atomic equilibrium positions in the given chiral structure. Taking account of this constraint, we have shown that the sound velocity of chiral phonons is identical independent of the sign of CAM m, and this disproves some precedent discussions expecting different velocities. Energy splitting $\Delta\omega$ between the $m = \pm 1$ CAM modes is remarkable for optical phonons, and it is linear in the phonon momentum k_z along the chiral axis as $\Delta\omega = \Gamma\, k_z\, m$ around $k_z = 0$. We have derived a simple formula for the coefficient Γ of this linear splitting represented in terms of microscopic stiffness constants in the dynamical matrix. This is a pseudo-scalar and corresponds to an electric toroidal monopole of the system.

In order to check this and further study the effects of chiral structure on phonon energy dispersion, we have also proposed a lattice model for which one can control its lattice chirality continuously. Its one limit is a set of three decoupled chiral tellurium-like lattices, while the other limit is a non-chiral coupled system with mirror symmetry. We have confirmed the above findings for the chiral system and found that the chirality-related energy splitting of optical phonons continuously vanish as we control the system towards the non-chiral limit. This type of energy splitting between two optical phonon modes had been recently observed by Raman scattering experiment, and the assignment of CAM quantum number was simultaneously performed to those two modes using the polarization selection rule [3], which is consistent with the theoretical predictions. We are planning to continue the study on chiral phonons and clarify other interesting properties related to several galvano-electric and galvano-magnetic responses.

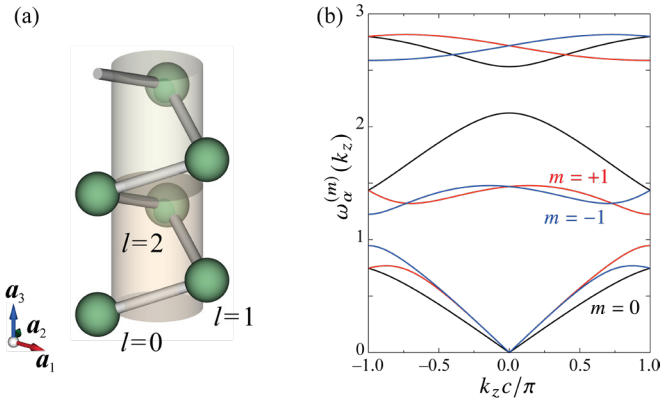

Fig. 1. (a) Structure of tellurium-like lattice. (b) Phonon energy dispersion in tellurium-like lattice for wave vector k = (0,0,k_z). m is the value of CAM. (Taken from Ref.[2]).

References
[1] S. Hayami, M. Yatsuhiro, Y. Yanagi, and H. Kusunose, Phys. Rev. B **98**, 165110 (2018).
[2] H. Tsunetsugu and H. Kusunose, J. Phys. Soc. Jpn. **92**, 023601 (2023).
[3] K. Ishito *et al.*, Nat. Phys. **19**, 35 (2023).

Authors
H. Tsunetsugu and H. Kusunose[a]
[a]Meiji University

PI of Joint-use project: H. Kusunose
Host lab: Tsunetsugu Group

Mechanical Conformation Control of Cyclized Binaphthyl at the Air–Water Interface

Biological activity is maintained by various molecular machines working in the body. The complex structure of molecular machines makes it difficult to elucidate their behavior. Molecular machines function through a combination of various molecular conformation changes. Detailed analysis of simple molecular conformation changes is expected to provide a deeper understanding of the operating mechanisms of complex molecular machines. The air-water interface is a suitable field for controlling molecular machines because mechanical compression can be applied with the help of movable barriers of the Langmuir–Blodgett (LB) system, comparable to those that can change the conformation of proteins. In addition, a lipid matrix, which is a medium analogous to biological membranes, can be prepared at the air-water interface.

Molecular conformations can be identified using several spectroscopic methods. We have confirmed the conformational change of binaphthyl derivatives at the air-water interface. The circular dichroism (CD) spectra can be obtained for these molecules at low concentrations and the spectra sensitively reflect conformational changes [1, 2]. In this work, we have controlled the molecular conformations of monobinaphthyldurene (MBD) in a lipid matrix similar to biological systems [3].

Figure 1 shows the chemical structure of MBD and three conformers of 1-MBD, 2-MBD, and flat-MBD, which is indicated by density functional theory (DFT) calculations, having different dihedral angles of φ between the two naphthyl moieties. The conformer 2-MBD is 2.8 kcal mol^{-1} higher in energy than the more stable 1-MBD, while flat-MBD is not favored energetically. DFT calculations also indicate that 2-MBD has a larger dihedral angle than 1-MBD, which causes the CD peak of 2-MBD to shift to a longer wavelength.

MBD was mixed with linear stearic acid (SA) or unsaturated oleic acid (OA) as matrices and then spread at the air–water interface. The mechanical properties of the mixed monolayers with MBD were characterized by surface pressure–molecular area (π-A) isotherms. The monolayers were transferred onto quartz substrates at different surface pressures to analyze the molecular aggregations and conformations by using CD spectra and Fourier transform infrared reflection absorption spectroscopy (FT-IR-RAS), atomic force microscopy (AFM). It suggested that MBD mixes more effectively with OA than with SA and dissolves in the lipid matrices upon mechanical compression.

The π–A isotherms suggest high miscibility of MBD with OA. It was also supported by FT-IR-RAS and AFM. The CD peak of the mixed monolayer with SA did not change with surface pressure. On the other hand, the mixed monolayer with OA shifted to longer wavelength with increasing surface pressure. Thus, the conformation of MBD changes from 1-MBD to 2-MBD in the mixed monolayer of OA; in contrast, 1-MBD is stable in SA. The higher-energy conformer 2-MBD is stabilized by the dissolution in the highly miscible lipids of OA.

As summarized in Figure 2, MBD confirmations could be controlled from 1-MBD to 2-MBD by mechanical stimulus in highly miscible lipids of OA. In contrast, the most stable 1-MBD conformation could not be transformed during mechanical compression in poorly miscible lipids of SA. It was found that different behaviors of molecular machines showed in their different local environments.

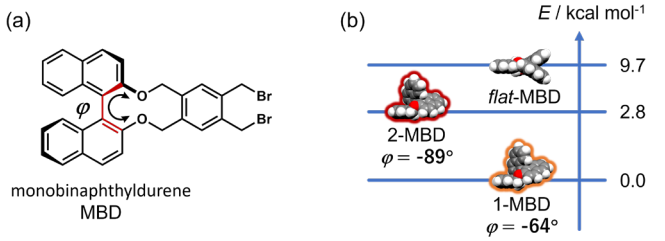

Fig. 1. (a) Molecular structure of MBD having a dihedral angle φ between two naphthyl rings of 1,1′-binaphthyl; (b) relative energies of MBD conformers.

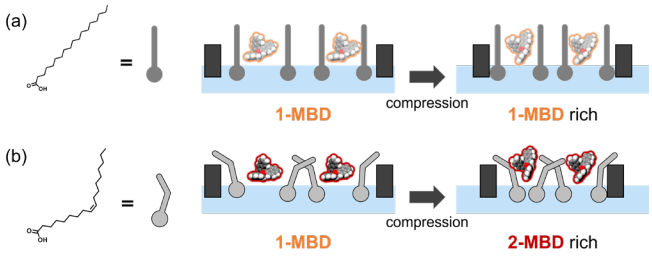

Fig. 2. Schematic Illustration of Aggregated States Involving MBD and Lipid Matrices. (a) Mixed with stearic acid. 1-MBD persists during mechanical compression; (b) mixed with oleic acid. MBD dissolves in oleic acid, accompanied by a conformational change from 1-MBD to 2-MBD.

References

[1] D. Ishikawa, T. Mori, Y. Yonamine, W. Nakanishi, D. L. Cheung, J. P. Hill, and K. Ariga, Angew. Chem. Int. Ed. **54**, 8988 (2015).
[2] M. Ishii, T. Mori, W. Nakanishi, J. P. Hill, H. Sakai, and K. Ariga, ACS Nano **14**, 13294 (2020).
[3] M. Ishii, T. Mori, W. Nakanishi, J. P. Hill, H. Sakai, and K. Ariga, Langmuir **38**, 6481 (2022).

Authors

M. Ishii[a,b], T. Mori, W. Nakanishi[b], J. P. Hill[b], H. Sakai[a], and K. Ariga[b]
[a]Tokyo University of Science
[b]National Institute for Materials Science

PI of Joint-use project: K. Ariga
Host lab: Lippmaa Group

Drude Weights in One-Dimensional Systems with a Single Defect

Ballistic transport of a quantum system can be characterized by Drude weight, which quantifies the response of the system to a uniform electric field in the infinitely long timescale. The Drude weight is often discussed in terms of the Kohn formula, which gives the Drude weight by the derivative of the energy eigenvalue of a finite-size system with the periodic boundary condition in terms of the Aharonov-Bohm flux. Recently, the Kohn formula is generalized to nonlinear responses [1,2]. In particular, for the S = 1/2 XXZ chain, analytic expressions of the nonlinear Drude weights are obtained utilizing the Bethe Ansatz exact solution. However, the nonlinear Drude weight determined by the Kohn formula often diverges in the thermodynamic limit. In order to elucidate the issue, in this work [3] we examine a simple example of a one-dimensional tight-binding model in the presence of a single defect at zero temperature. This problem can be formulated in terms of the scattering matrix of the defect. While the bulk energy density and the "defect energy" are

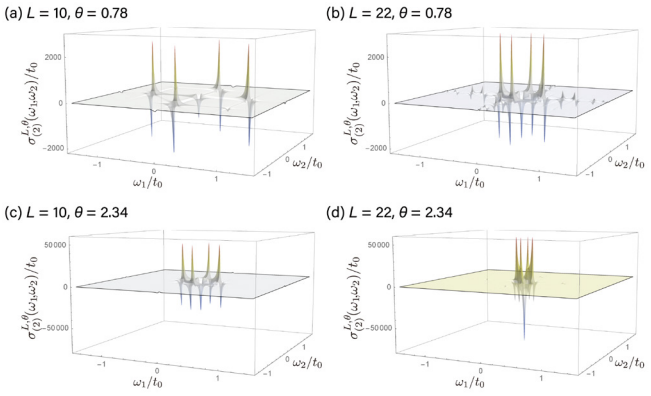

Fig. 1. Second-order optical conductivity of the impurity model for system size L=10, 22 with the Aharonov-Bohm flux θ, as a function of the two frequencies ω_1 and ω_2. Several peaks are observed near zero frequencies.

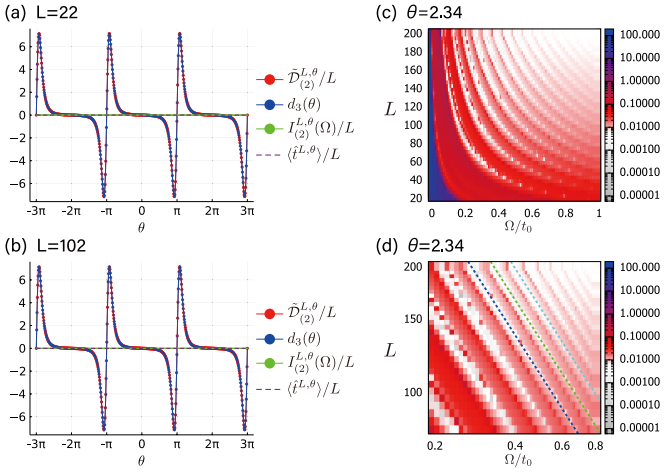

Fig. 2. Comparison between the Kohn formula $\tilde{\mathcal{D}}_{(2)}$ and the optical conductivity integrated over a window of low frequencies $I_{(2)}$, for the second-order Drude weight. While the Kohn formula depends strongly on the Aharonov-Bohm flux θ, the integrated conductivity (almost) vanishes for the entire range of θ. The latter corresponds to the vanishing bulk Drude weight expected in the thermodynamic limit.

non-universal and independent of the Aharonov-Bohm flux, the flux dependence appears in the O(1/L) correction, where L is the system size, which is a universal function of the scattering matrix. This is also consistent with the Conformal Field Theory. Using this formulation, we find that its linear and non-linear Drude weights given by the Kohn formula (i) depend on the Aharonov-Bohm flux and (ii) diverge proportionally to a power of the system size. Since the effect of the Aharonov-Bohm flux on the bulk transport property should vanish in the thermodynamic limit, the dependence on the Aharonov-Bohm flux signals that the non-linear Drude weights thus obtained may not describe the bulk property.

We argue that the problem can be attributed to different order of limits. The Drude weight according to the Kohn formula indicates the response of a finite-size system to an adiabatic insertion of the Aharonov-Bohm flux. While it is a well-defined physical quantity for a finite-size system, its thermodynamic limit does not always describe the ballistic transport of the bulk. The pathological behaviors such as the divergence of the nonlinear Drude weights mentioned above are indications of the discrepancy between the bulk transport property and the thermodynamic limit of the Kohn formula.

In order to clarify the issue, we propose to call the thermodynamic limit of the Kohn formula, namely the Drude weight defined by taking the adiabatic limit before the thermodynamic limit as "Kohn Drude weight". The ballistic transport of the bulk is rather characterized by the "bulk Drude weight" defined by taking the thermodynamic limit first before the adiabatic (zero-frequency) limit. While the potential issue of the order of limits has been sometimes discussed within the linear response, the discrepancy between the two limits is amplified in nonlinear Drude weights. We demonstrate that, the low-energy excitations of O(1/L) in the finite system of size L, which are excluded from the Kohn–Drude weight, contribute to the bulk Drude weight. This removes the pathological behaviors, making the bulk Drude weight finite and also independent of the Aharonov-Bohm flux.

References
[1] H. Watanabe and M. Oshikawa, Phys. Rev. B **102**, 165137 (2020).
[2] H. Watanabe, Y. Liu, and M. Oshikawa, J. Stat. Phys. **181**, 2050 (2020).
[3] K. Takasan, M. Oshikawa, and H. Watanabe, Phys. Rev. B **107**, 075141 (2023).

Authors
K. Takasan[a], M. Oshikawa, and H. Watanabe[a]
[a]University of Tokyo

PI of Joint-use project: K. Takasan
Host lab: Oshikawa Group

Perfect Co^{2+}-Based $J_{eff} = 1/2$ Kagomé Magnets

Kagomé lattice antiferromagnets have attracted significant interest in condensed matter physics due to their exotic magnetic properties, such as geometric frustration and the emergence of topologically ordered ground states. Our research aims to contribute to understanding the J_{eff} = 1/2 kagomé physics, which has not been comprehensively explored experimentally or theoretically. In this study, we report the synthesis, crystal structure, and magnetic properties of two cobalt-based kagomé magnets, namely $Co_3V_2O_7(OH)_2{\cdot}2H_2O$ and $BaCo_3(VO_4)_2(OH)_2$. These compounds can be considered as Co analogs of the extensively studied quantum kagomé magnets volborthite $Cu_3V_2O_7(OH)_2{\cdot}2H_2O$ and vesignieite $BaCu_3(VO_4)_2(OH)_2$. The titled Co^{2+}-based kagomé materials were synthesized utilizing the hydrothermal technique. For a comprehensive understanding of the specific synthesis procedures employed in this study, please refer to the associated publication [1].

As illustrated in Figure 1, the temperature-dependent magnetic susceptibility of $Co_3V_2O_7(OH)_2{\cdot}2H_2O$ and $BaCo_3(VO_4)_2(OH)_2$ under low magnetic fields of 10 mT displays anomalies indicative of an antiferromagnetic transition. However, this characteristic behavior vanishes when the applied magnetic field is elevated to 0.1 T. This observation can be corroborated by the isothermal magnetization process at 2 K, depicted in Figure 2(a), where the antiferromagnetic ground state is suppressed by a field-induced phase transition at considerably lower magnetic fields (75 mT for $Co_3V_2O_7(OH)_2{\cdot}2H_2O$ and 16 mT for $BaCo_3(VO_4)_2(OH)_2$, respectively). Moreover, the M^2 vs. H/M plot [Figure 2(b)] reveals a curve characteristic of metamagnetism. In the high-field region beyond the metamagnetic transition field, the M^2 vs. H/M plot exhibits linearity, signifying that the order parameter within the framework of Landau theory corresponds to the spontaneous magnetization M_0 (associated with the value of the intercept) and exhibits a metamagnetic feature [2].

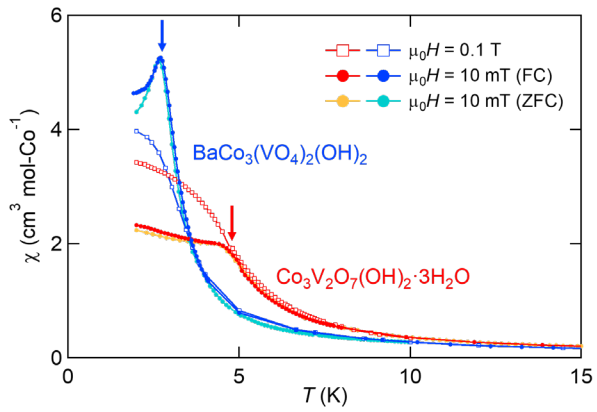

Fig. 1. Temperature dependence of magnetic susceptibility (χ) in Co^{2+}-based kagomé magnets, measured under magnetic fields of 0.1 T and 10 mT.

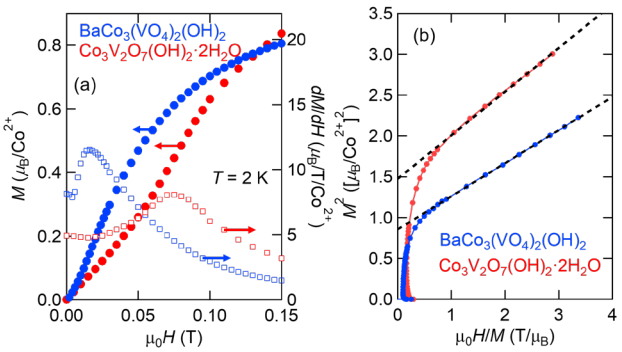

Fig. 2. (a) Low-field (< 0.15 T) magnetization curves (M) and their derivatives (dM/dH) obtained at 2 K for Co^{2+}-based kagome magnets. A metamagnetic-like transition is discerned at μ_0H = 75 mT for $Co_3V_2O_7(OH)_2{\cdot}2H_2O$ and μ_0H = 16 mT for $BaCo_3(VO_4)_2(OH)_2$. (b) The M^2 vs. μ_0H/M plot

Nevertheless, the spontaneous magnetization M_0 is approximately half of the powder-averaged saturation magnetization of 2 μ_B anticipated for Co^{2+} and cannot be elucidated by simple in-plane ferromagnetism, as typically observed in metamagnetic transitions. Theoretical investigations suggest that antisymmetric exchange mediated by the Dzyaloshinsky-Moriya (DM) interaction may engender such moments by causing a slight out-of-plane tilt of the spins [3,4]. The DM interaction prompts the spins within each triangle of the kagomé lattice to adopt an "umbrella" configuration [5]. If the Co^{2+} ion exhibits a J_{eff} = 1/2 effective spin, the powder-averaged g factor is approximately 4. The angle θ, representing the spin tilt induced by the DM interaction, is nearly equal to arctan[(g-2)/g]. Consequently, the emergent ferromagnetic moment in Co^{2+} spin is approximately 45% of the saturation magnetization, which explains the magnetic moment that emerges due to the metamagnetic transition, constituting nearly half of the saturation field.

Based on these observations, the origin of the metamagnetic transition in Co^{2+} kagomé systems can be elucidated as portrayed in Figure 3. The relatively substantial DM interaction provokes each triangular spin of the kagomé lattice to adopt a significantly tilted umbrella structure, generating a ferromagnetic moment of about $M_0 \sim 1$ μ_B on each kagomé plane. The coupling between kagomé planes is characterized by weak antiferromagnetic interactions between layers of ferromagnetic moments under a feeble applied magnetic field. Furthermore, the antiferromagnetic coupling becomes destabilized by weak magnetic fields on the order of tens of millitesla, culminating in "halfway-saturated ferromagnetism."

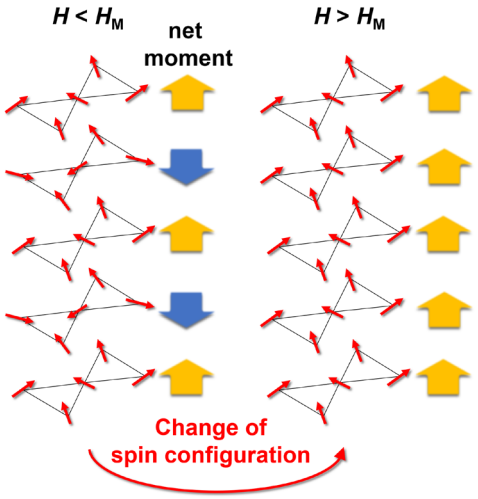

Fig. 3. Schematic representation of the spin configuration transition in Co^{2+}-based kagomé magnets, wherein antiferromagnetically aligned canted moments transform into ferromagnetically aligned ones.

Our study highlights the importance of synthesizing and characterizing new materials with kagomé lattice structures to broaden the understanding of the J_{eff} = 1/2 kagomé physics. Furthermore, the Co^{2+} kagomé magnets presented here serve as a platform for further investigations of the interplay between crystal-field, superexchange, spin-orbit coupling, and DM interactions in kagomé systems.

References

[1] Y. Haraguchi, T. Ohnoda, A. Matsuo, K. Kindo, and H. Aruga Katori, Physical Review B **106**, 214421 (2022).
[2] S. K. Banerjee, Phys. Lett. **12**, 16 (1964).
[3] I. E. Dzyaloshinskii, J. Phys. Chem. Solids **4**, 241 (1958).
[4] T. Moriya, Phys. Rev. **120**, 91 (1960).
[5] M. Elhajal, B. Canals, and C. Lacroix, Phys. Rev. B **66**, 014422 (2002).

Authors
Y. Haraguchi[a], T. Ohnoda[a], A. Matsuo, K. Kindo, and H. Aruga Katori[a]
[a]Tokyo University of Agriculture and Technology

PI of Joint-use project: Y. Haraguchi
Host lab: Hiroi Group and Electromagnetic Measurements Section

Unconventional Superconductivity Robust Against Impurities in a Newly Discovered Kagome Lattice Superconductor

One of the strategies in the search for quantum phenomena such as non-trivial magnetism and superconductivity is to focus on the symmetry of crystal structures of materials. The kagome lattice consisting of corner-sharing triangles and hexagonal holes (Fig. 1(a)) has attracted much attention because materials with kagome lattice structures exhibit various exotic properties, such as quantum spin liquids, Dirac/Weyl physics, and unconventional superconductivity, driven by its geometry. In this context, the discovery of superconductivity in AV_3Sb_5 (A = K, Rb, Cs) with a perfect kagome lattice in 2020 has received significant attention [1]. In these materials, charge density wave (CDW)

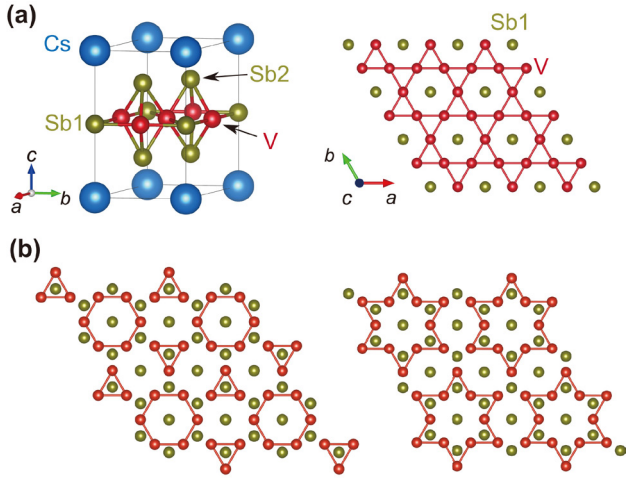

Fig. 1. (a) Crystal structure of CsV_3Sb_5. V-Sb1 plane viewed from the c-axis direction (right). Whereas the V atoms form a two-dimensional kagome network, the Sb1 atoms are located at the hexagonal centers.(b) CDW pattern in CsV_3Sb_5. V and Sb1 atoms form the so-called star of David (right) and inverse star of David (left) patterns. These patterns alternate in the interplane direction.

orders with a so-called (inverse) star-of-David pattern of electronic hopping have been observed above the superconducting transition temperature (Fig. 1(b)) [2]. Very interestingly, it has been reported that these CDW states break time-reversal and rotational symmetries. In addition, high-pressure studies have revealed that the CDW phase is suppressed by applying pressure, accompanied by the emergence of a superconducting dome, indicating the close relationship between the CDW and superconductivity [3,4]. Therefore, one of the most crucial unresolved issues is identifying the symmetry of the superconductivity that develops inside the CDW phase. However, the mechanism of superconductivity in AV_3Sb_5 and its relationship with the CDW state have remained elusive [2].

Here, we focus on the effect of impurities on the superconducting state to elucidate the mechanism of superconductivity in AV_3Sb_5. Based on the Bardeen-Cooper-Schrieffer (BCS) theory, which is the standard theory of superconductivity, the conventional superconducting state arises from the pairing of two electrons induced by electron-phonon interactions. In this case, the introduction of nonmagnetic impurities generally has little effect on the superconducting transition temperature (T_c) and the superconducting gap structure [5]. However, it is well known that unconventional superconducting states, as observed in high-T_c cuprates and heavy-fermion superconductors, are significantly suppressed by nonmagnetic impurities.

In this study, we systematically investigated the impurity effects of CsV_3Sb_5 on the superconducting transition temperature and the superconducting gap structure [6]. The introduction of non-magnetic impurities into crystals was achieved by using electron irradiation, enabling precise control of the impurity concentration in the CsV_3Sb_5 single-crystal samples. We examined the change in the superconducting transition temperature by measuring the resistivity of the impurity-controlled samples at ambient and high pressure. We also performed magnetic penetration depth measurements, which reflect the superconducting gap structure. As a result, we found that the superconducting transition temperature of CsV_3Sb_5 is rapidly suppressed at a low impurity concentration but starts to saturate at moderate impurity concentrations (Fig. 2(a)). This behavior differs from those of both conventional BCS superconductors and unconventional superconductors such as high-T_c cuprates. In addition, our magnetic penetration depth measurements

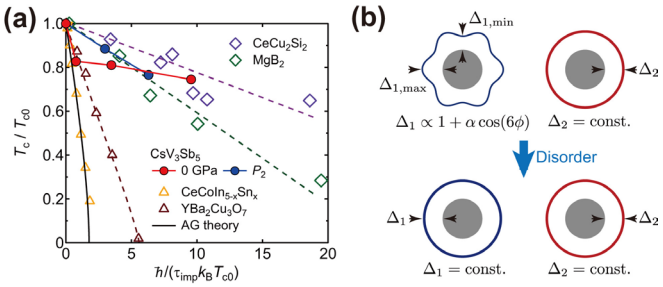

Fig. 2. (a) Suppression of the superconducting transition temperature T_c in CsV_3Sb_5 as a function of pair breaking parameter (corresponding to the amount of impurities). Red circles represent the transition temperature under ambient pressure (0 GPa), and blue circles represent the transition temperature at P_2. (b) Changes in the superconducting gap structure in CsV_3Sb_5 by impurities. The gap structure is anisotropic before the introduction of impurities, but as the impurity concentration is increased, the gap size averages out and eventually the two gaps become isotropic and almost the same size. This behavior is consistent with the theoretical expectation in the bond-order fluctuation superconducting mechanism [6].

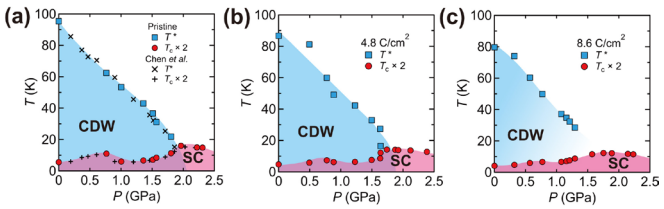

Fig 3. P-T phase diagrams of the (a) pristine, (b) 4.8, and (c) 8.6 C/cm^2 irradiated samples. For clarity, T_c is doubled. The phase diagram of the pristine sample includes data from Chen *et al* [3]. The CDW (superconducting (SC)) phase is shaded in blue (red).

reveal that with increasing impurities, an anisotropic fully-gapped state changes to an isotropic full-gap state without showing impurity-induced Andreev bound states, which excludes any of sign-changing symmetries (Fig. 2(b)). Furthermore, transport measurements under pressure show that the double superconducting dome in the pressure-temperature phase diagram survives against sufficient impurities (Fig. 3). These results support that CsV_3Sb_5 is a non-chiral, anisotropic *s*-wave superconductor with no sign change both at ambient and under pressure. The present findings support a new type of unconventional superconductivity originated from bond-order fluctuations in the CDW state of CsV_3Sb_5, where the gap function is non-sign-changing *s*-wave [7].

Our present study will pave the way to understanding the unique electronic and superconducting states in kagome lattice materials.

References

[1] B. R. Ortiz *et al*., Phys. Rev. Lett. **125**, 247002 (2020).
[2] T. Neupert *et al*., Nat. Phys. **18**, 137 (2022).
[3] K. Y. Chen *et al*., Phys. Rev. Lett. **126**, 247001 (2021).
[4] R. Gupta *et al*., Commun. Phys. **5**, 232 (2022).
[5] P. W. Anderson, J. Phys. Chem. Solids **11**, 26 (1959).
[6] M. Roppongi *et al*., Nature Communications **14**, 667 (2023).
[7] R. Tazai *et al*., Sci. Adv. **8**, eabl4108 (2022).

Authors

M. Roppongi[a], K. Ishihara[a], K. Hashimoto[a], and T Shibauchi[a], and Y. Uwatoko
[a]The university of Tokyo

PI of Joint-use project: K. Hashimoto
Host lab: Uwatoko Group

Heavy-Fermion Antiferromagnet $Yb_4Ru_7As_6$ with the $U_4Re_7Si_6$ Type Cubic Structure

Yb–T–X (T: transition metal, X: pnictogen) ternary compounds have been studied intensively in terms of novel phenomena in the vicinity of the magnetic quantum critical point (QCP). For example, $YbNi_4P_2$ is reported to be close to the ferromagnetic QCP, exhibiting the ferromagnetic transition (FM) at 0.17 K [1]. The field-induced non-Fermi liquid behavior of $Yb_2Fe_{12}P_7$ has also attracted attention [2].

To our knowledge, no ternary compound of Yb–Ru–As has been reported. In this study, we have investigated ternary Yb–Ru–As compounds and found a compound $Yb_4Ru_7As_6$, which crystallizes in the $U_4Re_7Si_6$-type cubic structure, showing a weak ferromagnetic (FM) behavior below $T_0 \sim$ 4.0 K and antiferromagnetic (AFM) ordering at T_N = 2.5 K with the moderately enhanced electronic specific heat coefficient of 120 Yb-mJ/K^{2}mol [3].

Single crystals of $Yb_4Ru_7As_6$ were grown by the Bi-flux method, and obtained crystals are shown in the inset of Fig. 1. The crystal structure of $Yb_4Ru_7As_6$ is determined to be the cubic $U_4Re_7Si_6$-type structure (No.229, $Im\bar{3}m$) using a XtaLAB HyPix-600HE diffractometer. Note that the local symmetry of Yb atom is similar to rare earth metals in skutterudite. Fig. 1 shows the temperature dependence of the electrical resistivity ρ of $Yb_4Ru_7As_6$ for the current J along the [100] direction. With decreasing temperature, ρ monotonically decreases with a shoulder-like structure below 10 K. At low temperatures, two inflection points at T_0~4 K and T_N~2.5 K in ρ are observed, as shown in the inset of Fig. 1. The residual resistivity ratio is about 40, indicating a high-quality sample.

Magnetic properties are isotropic reflecting the cubic structure. With decreasing temperature, magnetic susceptibility M/H increases and follows the Curie–Weiss law at temperatures higher than 150 K. The estimated effective magnetic moments are 4.28–4.45 μ_B/Yb, which is close to the expected value of Yb^{3+} ionic state: 4.54 μ_B/Yb. Fig. 2 shows the temperature dependences of M/H for H || [100] below 10 K measured at several magnetic fields. M/H at 5 mT shows a ferromagnetic increment in the temperature range between 6 and 4 K, and a small peak at 2.5 K. Note that no detectable hysteresis loop is observed in magnetization at 1.8 K, as shown in the inset of Fig. 2. With increasing temperature, the peak temperature decreases to 2.25 K at 1.0 T and disappears above 2.0 T, meaning that the peak in M/H corresponds to the AFM transition.

The specific heat C shows an upturn below 7.5 K and λ type sharp peak at 2.5 K, corresponding to the short-range magnetic correlation and/or the Kondo effect, and the long-range magnetic ordering, respectively. In addition, a tiny anomalous behavior is observed at T_0~4 K, which corresponds to the temperature where the anomaly in ρ and the occurrence of the FM behavior emerge as mentioned above. It means that T_0 can be attributed to a temperature characterizing the FM behavior. T_N is shifted to lower temperatures under magnetic fields and seems to disappear at 2.5 T. On the other hand, the tiny anomaly at T_0 becomes obscure in the magnetic fields.

The characteristic temperature where the FM behavior in M/H is observed corresponds to the beginning of the short-range ordering as observed in the temperature dependence of C, implying that one of the possibilities of the FM in $Yb_4Ru_7As_6$ is considered a concomitant phenomenon of the AFM ordering with a canted magnetic moment arrangement from the <100> direction. The canted AFM can be realized in the condition of magnetic interaction and magnetocrystalline anisotropy favoring the non-antiparallel arrangement of magnetic moments. Since there is no inversion symmetry at the center between the nearest neighbor magnetic Yb sites, the Dzyaloshinskii–Moriya interaction can be one of the possible origins of FM behavior, for example. To elucidate the origin of T_0, resistivity measurements in magnetic fields are in progress, and further experiments with microscopic probes are needed.

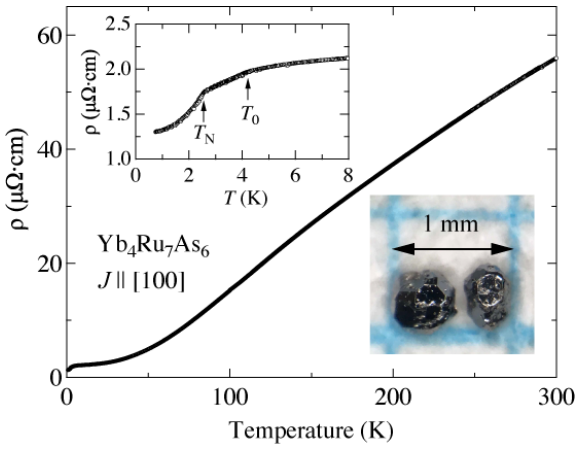

Fig. 1. Temperature dependence of ρ of $Yb_4Ru_7As_6$. The magnification of the low temperature part and photograph of single crystals are shown in inset.

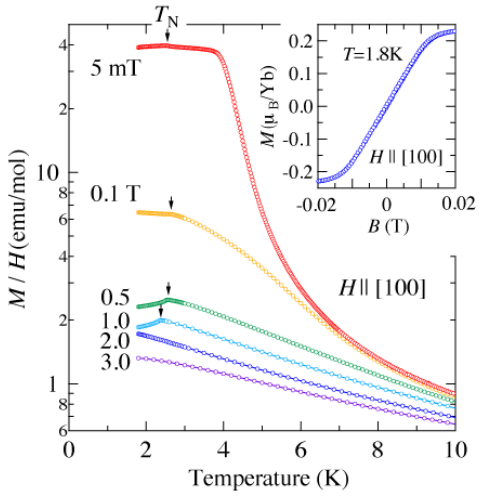

Fig. 2. M/H for H || [100] below 10 K at several magnetic fields. Inset shows the magnetization curve for H || [100] at 1.8 K in low magnetic fields.

References

[1] C. Krellner, S. Lausberg, A. Steppke, M. Brando, L. Pedrero, H. Pfau, S. Tencé, H. Rosner, F. Steglich, and C. Geibel, New J. Phys. **13**, (2011) 103014.

[2] R.E. Baumbach, J.J. Hamlin, L. Shu, D.A. Zocco, J.R. O'Brien, P.-C. Ho, and M.B. Maple, Phys. Rev. Lett. **105**, 106403 (2010).

[3] Y. Hirose, K. Arakawa, Y. Kato, Y. Uwatoko, H. Ma, J. Gouchi, F. Honda, and R. Settai, J. Magn. Magn. Mater. **556**, 169327 (2022).

Authors

Y. Hirose[a], K. Arakawa[a], Y. Kato[a], Y. Uwatoko, H. Ma, J. Gouchi, and F. Honda[b], R. Settai[a]

[a]Niigata University

[b]Kyushu University

PI of Joint-use project: Y. Hirose

Host lab: Uwatoko Group

Structural Instability and Electronic Properties of CeCoSi under Pressure

We have clarified structural and electronic properties under pressure at low temperatures on CeCoSi, which has been attracted attention for its novel long-range order. CeCoSi crystallizes into the tetragonal crystal structure (No. 129, P4/nmm), which lacks local inversion symmetry at Ce site. CeCoSi exhibits a long-range ordering below T_0 ~ 12 K at ambient pressure, which is proposed to be odd-parity multipole orderings. The T_0 strongly enhances with increasing pressure and reaches 37 K at 1.7 GPa, followed by a rapid suppression. The phase below T_0 is phase II and the phase II disappears above 2.2 GPa. CeCoSi also undergoes structural transition at P_s ~ 4.9 GPa at 300 K and becomes phase IV [1]. The rapid change of T_0, followed by the emergence of phase IV indicates that Ce-4f electronic state significantly altered under pressure. In order to reveal

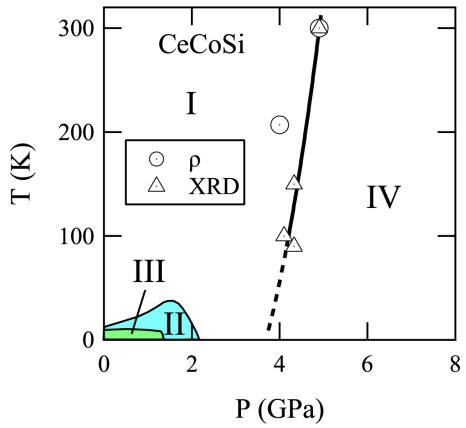

Fig. 1. Temperature Pressure phase diagram of CeCoSi. The bordering temperature and pressure are defined from resistivity (circle) and from XRD (triangle) measurements. The borders among phase I, II, III are in literature.

the electronic and structural properties of CeCoSi in the above whole temperature and pressure range and to clarify the relationship between phase II and IV, electrical resistivity of CeCoSi in the pressure range of 0 ~ 8 GPa and in the temperature range of 2.5 ~ 300 K and X-ray diffraction in 0 ~ 6 GPa and in 6 ~ 300 K have been performed.

CeCoSi single crystals were grown with a Ce/Co eutectic flux method. The electrical resistivity on CeCoSi has been performed by cubic anvil pressure system with a standard four terminal method. X-ray diffraction (XRD) on powdered CeCoSi has been performed with GM refrigerator incorporated with diamond anvil pressure cell [2].

Figure 1 shows the phase diagram depicted based on the results of electrical resistivity and XRD under pressure. The anomaly of electrical resistivity is observed as drop of resistivity by the temperature or pressure, whereas additional peaks and peak splittings are observed in the XRD pattern. This study reveals that the boundary of phase IV and phase I is not directly connected to phase II or phase III.

The temperature dependence of resistivity exhibits a peak due to the Kondo scattering of the conduction electrons. The temperature of this peak rapidly increases with increasing pressure, which corresponds the rapid enhancement of Kondo temperature under pressure. Although CeCoSi is reported as localized electronic state at ambient pressure, the results of resistivity suggest that CeCoSi becomes itinerant electronic state around 2 GPa. XRD indicates that the ratio of lattice parameters *c/a* of CeCoSi linearly decreases with pressure up to ~ 4 GPa, which is just below P_s. In contrast, *c/a* of LaCoSi and PrCoSi decreases linearly below 2 GPa but they level off above 2 GPa. These results suggest that the valence of Ce on CeCoSi gradually increases from 3+ above 2 GPa. Also, the resistivity shows a drop to exhibit a metallic temperature dependence when crossing the phase IV.

These results strongly suggest that CeCoSi is localized character at ambient pressure and it gradually becomes itinerant character around 2 GPa and the valence of Ce gradually changes above 2 GPa. In addition, the Ce-4f electronic states changes drastically when crossing the boundary of phase I and IV, implying the valence change by the structural transition. Although phase II and IV is not directly influenced to each other, our results strongly suggest that both the rapid change of T_0 and emergence of phase IV can be ascribed to the valence instability of Ce-4f electron.

References
[1] Y. Kawamura *et al*., J. Phys. Soc. Jpn. **89**, 054702 (2020).
[2] Y. Kawamura *et al*., J. Phys. Soc. Jpn. **91**, 064714 (2022).

Authors
Y. Kawamura[a], K. Ikeda[a], J. Hayashi[a], K. Takeda[a], C. Sekine[a], T. Matsumura[b], J. Gouchi, Y. Uwatoko, T. Tomita, H. Takahashi[c], and H. Tanida[d]
[a]Muroran Institute of Technology
[b]Hiroshima University
[c]Nihon University
[d]Toyama Prefectural University

PI of Joint-use project: Y. Kawamura
Host lab: Uwatoko Group

Sub-Micron Particle Size Effects on Metastable Phases for a Photoswitchable Co-Fe Prussian Blue Analogue

The $K_{0.3}Co[Fe(CN)_6]_{0.77}\cdot nH_2O$ compound undergoes a charge transfer coupled spin transition (CTCST), where spin configurations change between a paramagnetic Co^{II} (S = 3/2)-Fe^{III} (S = 1/2) high temperature (HT) state and a diamagnetic Co^{III} (S = 0) -Fe^{II} (S = 0) low temperature (LT) state. The compound having average particle size of 500 nm exhibits a unique intermediate **(IM)** phase that depend on the cooling rate. The IM phase corresponds to a mixture of IM-A (HT+LT fraction mixture) and IM-B (LT state), which have ~50 nm and ~200 nm coherent domain sizes, receptivity [1]. (Fig. 1) Moreover, several hidden metastable HT states

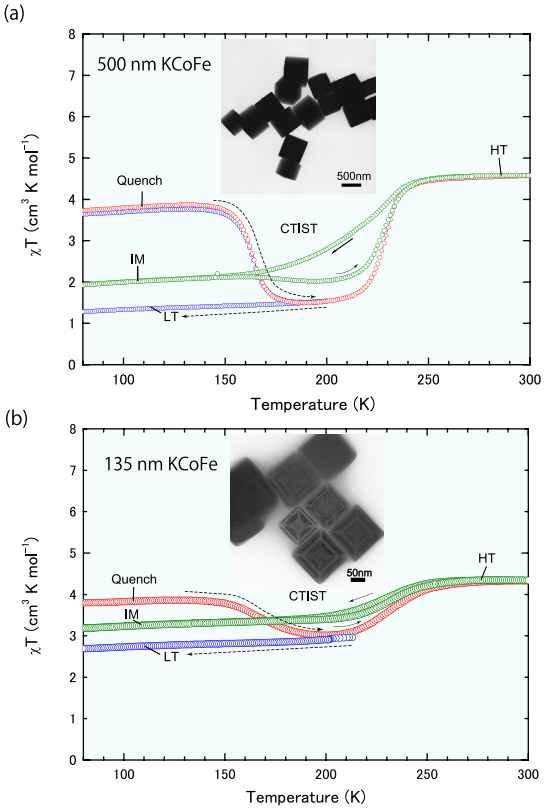

Fig. 1. Magnetic susceptibility curves of $K_{0.3}Co[Fe(CN)_6]_{0.77}\cdot nH_2O$ for (a) 500 nm and (b) 135 nm particles. The thermally accessed Quench (Q) phase and Low-temperature (LT) phase are depicted as red and blue curves, respectively. The thermal procedure to reach the LT phase is indicated by dotted arrow. The IM phase is obtained by slow cooling (at 1 K/min). Differences in the thermal response as a function of particle size are observed in the hysteresis, becoming narrower with decreasing particle size. Insets: TEM images of the particles showing their clear cubic shapes.

emerge as a function of thermal and photo stimuli in the compound, namely: (1) a quench (**Q**) state generated from the HT state by flash cooling, (2) a **LTPX** state obtained by photoexcitation from the LT state derived by thermal relaxation from the Q state, and (3) an **IMPX** state accessed by photo-irradiation from the IM state [1, 2]. (Fig. 2(a))

A sample with smaller particle size 135 nm, which were designed on the scale of the coherent LT domains in the IM phase of the 500 nm sample [3], was investigated for by means of thermal and photo controlled PXRD and complementary magnetic susceptibility measurements, and an unusual IM phase and metastable HT phases in 135 nm particles of $K_{0.3}Co[Fe(CN)_6]_{0.77}\cdot nH_2O$ were compared to those of a similar sample with 500 nm particle size in the paper (Fig. 2). The incomplete character of the thermally-induced CTCST between Co^{II} (S = 3/2)-Fe^{III} (S = 1/2) and Co^{III} (S = 0)-Fe^{II} (S = 0) pairs becomes even less complete when the particle size is reduced from 500 nm to 135 nm. The HT spin Co^{II}-Fe^{III} states become predominant and the PXRD profiles suggest a multiphasic behavior, with a peak broadening larger than the one observed for the 500 nm sample. This behavior is attributed to HT domains or clusters made of a limited number of Co^{II}-Fe^{III} pairs that become constrained within the Co^{III}-Fe^{II} lattice at low temperature, which compose a multitude of Co^{II}-Fe^{III} clusters having different sizes and experiencing different elastic strains from the dominant Co^{III}-Fe^{II} phase. The multiple state in IM phase can be then viewed as a response of an inhomogeneous diluted system. In addition, the disordered character generated by CTCST in the 135 nm sample reflects to LT state obtained by thermal relaxation from a single Q phase and photo-excited states from IM and LT states, these metastable phases are always multiple states. (Fig. 2(b))

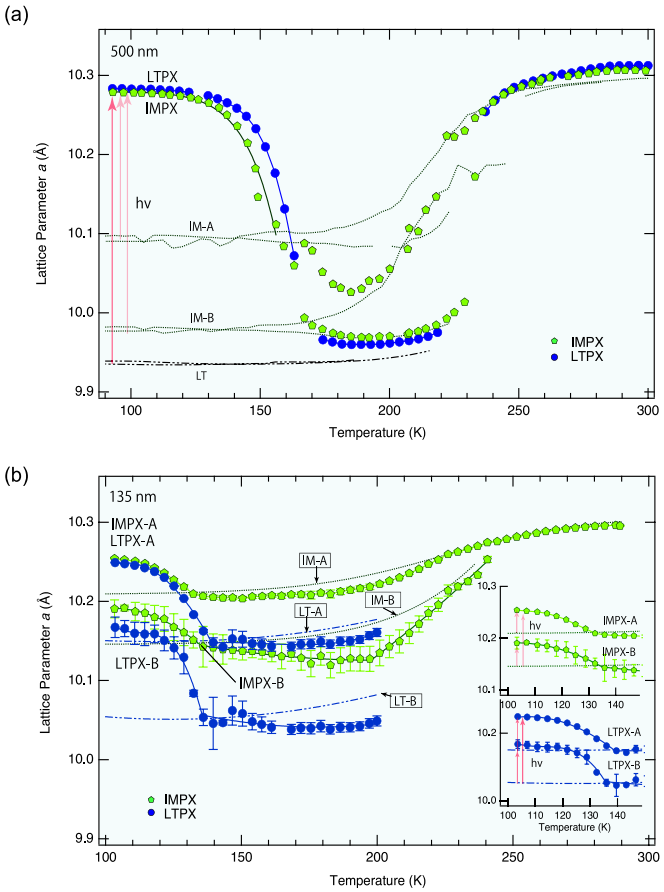

Fig. 2. Thermal decay of the lattice parameter *a* for photo-excited states IMPX (filled pentagons) and LTPX (filled circles) produced from IM and LT states, at 90 K for the 500 nm sample and at 100 K for the 135 nm sample. (a) Data related to the 500 nm sample extracted by the Le Bail method. The original IM state and LT state, which are the starting phases before 690 nm light irradiations, are indicated by the dotted and dot-dash lines, respectively. (b) Similar plots for the 135 nm sample extracted from (400) PXRD peaks. Inset: Expanded figures between 100 K and 150 K for temperature dependent photo-excited lattice parameters, IMPX-A & B (filled pentagons) and LTPX-A & B (filled circles) from the respective original states, IM-A &B (dotted lines) and LT-A & B (dot-dash lines).

Determination of the linear thermal expansion coefficients (LTEC) and pressure- dependent CTCST temperatures for the two (500 nm and 135 nm) particle sizes gave insights on the intrinsic stretchability and external compressibility, which were indicated that the bulk sample has higher flexibility at the CTCST, while the lattice change at the CTCST becomes less sensitive to external circumstances upon size reduction. We attributed these behaviors to the decrease of the cooperative electron-phonon coupling in small particles due to the enhancement of lattice defects which alters the elasticity of the small particles. The weak character of the elastic energy barriers produced during photoexcitation, combined with the disorder of elastic forces in the lattice, prevents the complete photoexcitation and the collective lattice change in the 135 nm sample. As a result, in the $K_{0.3}Co[Fe(CN)_6]_{0.77}\cdot nH_2O$ compound, photo-excitation under common values of power density does not change from the multiphasic IM state and/or LT state to a single metastable HT phase, through sub-micron scale particle size reduction [4].

References

[1] C. Chong, M. Itoi, K. Boukheddaden, E. Codjovi, A. Rotaru, F. Varret, F. A. Frye, D. R. Talham, I. Maurin, D. Chernyshov, and M. Castro, Phys. Rev. B. **84**, 144102 (2011).
[2] M. Itoi, I. Maurin, F. Varret, F. A. Fry, D. R. Talham, D. Chernyshov, and K. Boukheddaden, Phys. Rev. B. **88**, 094104 (2013).
[3] M. J. Andrus, Y. M. Calm, E. S. Knowles, M. F. Dumont, K. A. Abboud, M. W. Meisel, and D. R. Talham, Polyhedron **64,** 289 (2013).
[4] M. Itoi, I. Maurin, K. Boukheddaden, M. J. Andrus, D. R. Talham, E. Elkaim, and Y. Uwatoko, J. Appl. Phys. **131**, 085110 (2022)

Authors

M. Itoi[a], I. Maurin[b,c], K. Boukheddaden[d], M. J. Andrus[e], D. R. Talham[e], E. Elkaim[f], and Y. Uwatoko

[a]Nihon University School of Medicine
[b]Ecole Polytechnique
[c]Institut NEEL
[d]Université de Versailles-Saint-Quentin
[e]University of Florida
[f]Synchrotron SOLEIL

PI of Joint-use project: M. Itoi
Host lab: Uwatoko Group

Conformation of Ultra-Long Chain Fatty Acid in Lipid Bilayer

Phospholipids are the most abundant lipids in biological membranes and have a polar head group and two hydrocarbon tails (fatty acids). Phospholipids, more than 1000 molecular species, are biosynthesized by a combination of a head group and two hydrocarbon tails. Each tail typically contains between 14 and 22 carbon atoms. Fatty acids containing more than 22 carbons are called very-long-chain fatty acids, such as docosahexaenoic acid (DHA, C22:6). Moreover, much longer chains containing more than 32 carbons were found at the sn-1 position of phosphatidylcholine in photoreceptors, fibroblasts, and keratinocytes. These fatty acids are called ultra-long-chain fatty acids (ULCFAs). It is considered that ULCFAs are stored as a precursor of

bioactive lipid mediators and derivatives of C32:6 and C34:6 are neuroprotective in retina. However, the physicochemical properties of ULCFAs and the biological roles of ULCFAs-containing phospholipids are still unclear. In order to clarify the physicochemical properties of ULCFAs, we have simulated a single ULCFA in a lipid bilayer by all-atom molecular dynamics using the ISSP supercomputer [1,2].

We found that ULCFAs have large conformational fluctuations. Figure 1 shows the conformations of dotriacontahexaenoic acid containing phosphatidylcholine (dTSPC, C32:6-C18:0) in membrane of distearoyl phosphatidylcholine (DSPC, C18:0-C18:0) [1]. The ultra-long chain has a turned conformation in the upper leaflet, a L-shaped conformation between the two leaflets, and an elongated conformation deeply inserting in the lower (opposite) leaflet. The L-shaped conformation is taken most frequently. There are no free-energy barriers among these conformations and the transit time between turned and elongated conformations is ~ 10 ns. Moreover, we revealed that ULCFAs can sense the density differences between the two leaflets and respond to these changes. As the number ratio of lipids in the opposite leaflet increases, the ratio of the elongated shape linearly decreases. This change in ULCFA conformations reduces the lipid-density difference between the two leaflets. We have examined three types of phospholipids (DSPC, SDPC, C18:0-C22:6, and SOPC, C18:0-C18:1) for host membranes and three types of ULCFAs (dTSPC, HSPC, C26:4-C18:0, and LSPC, C32:0-C18:0) [1,2]. HSPC is constructed by truncating the long hydrocarbon chain of dTSPC at C26, and LSPC is constructed by the saturation of the long hydrocarbon chain of dTSPC. In all cases, ULCFAs have this sensing capability. Therefore, we concluded that it is a unique property of ULCFAs. This response may be essential for the functions of ULCFAs in living cells.

Moreover, we added cholesterols to membranes [2]. The flip—flop of cholesterols is ~1 μs and is much faster than those of phospholipids (hours or days). The flip—flop of cholesterols can also reduce the lipid-density difference. After the equilibration of cholesterols, the probability distribution of ULCFA conformations is back to that for no-lipid-density-difference membranes. Thus, we consider that ULCFAs initially respond to the density difference and, later, cholesterol removes the difference in living cells.

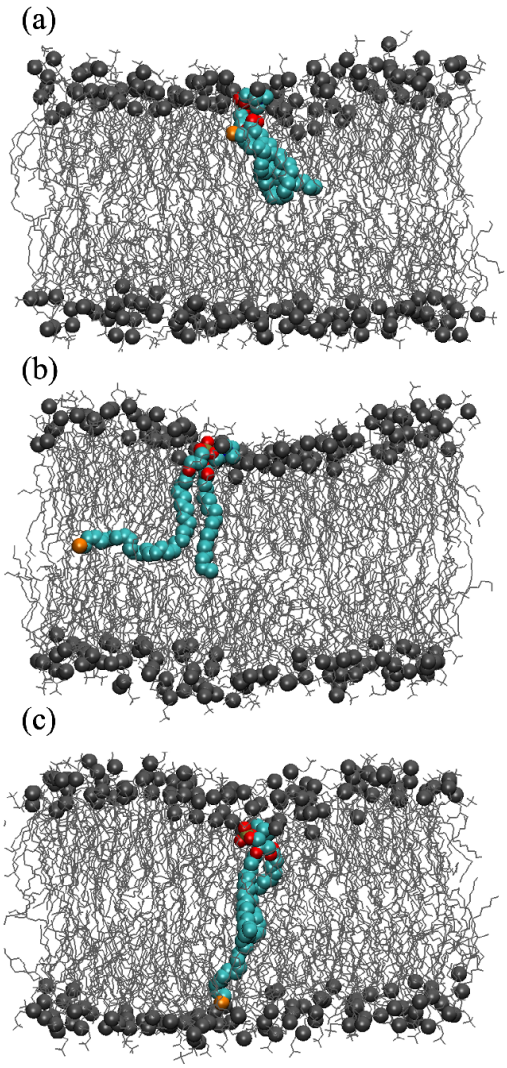

Fig. 1. Snapshots of a Ultra-Long Chain Fatty Acid, dTSPC, in bilayer membrane. (a) Turned conformation. (b) L-shaped conformation. (c) Elongated conformation. dTSPC are represented by colored spheres. Host lipid (DSPC) molecules are shown in gray (spheres represent the phosphate atoms). Water molecules are not shown for clarity.

References
[1] K. Kawaguchi, K. M. Nakagawa, S. Nakagawa, H. Shindou, H. Nagao, and H. Noguchi, J. Chem. Phys. **153**, 165101 (2020).
[2] K. Kawaguchi, H. Nagao, H. Shindou, and H. Noguchi, J. Phys. Chem. B **126**, 9316 (2022).

Authors
K. Kawaguchi[a] and H. Noguchi
[a]Kanazawa University

PI of Joint-use project: K. Kawaguchi
Host lab: Noguchi Group

Unified View of High-T_c Superconductivity and Quantum Spin Liquids Revealed by *Ab initio* Supercomputer Simulations

Since the discovery of superconductivity in 1986 in copper oxides with quasi-two-dimensional perovskite structure, more than 35 years have already passed. However, its mechanism has not converged to consensus in the community because of the difficulty in treating strongly correlated electron systems, to which the cuprates belong.

Recently, numerical methods to study the strongly correlated electron systems have largely been developed [1], in which effective Hamiltonians derived by an *ab initio* framework starting from given crystal structure without resorting to adjustable parameters are solved by accurate quantum many-body solvers. The solutions of effective Hamiltonians for a number of copper oxide compounds correctly reproduce *d*-wave superconducting ground states [2,3]. From the relation between the *ab initio* parameters and the obtained superconducting order parameters, the principal component that controls the strength of the superconductivity was found. The results further show that the diverse materials dependence is well captured as shown in Fig. 1 for the superconducting critical temperature T_c. It was also clarified how the superconductivity can be enhanced in the present mechanism beyond the existing materials.

The *ab initio* solution also offers insights into electron fractionalization. It was found that an electron that is an elementary particle in vacuum is emergently splintered in strongly correlated electron systems. Thus generated particles are mutually tunneling quantum mechanically, in other words, hybridizing each other. The fractionalization

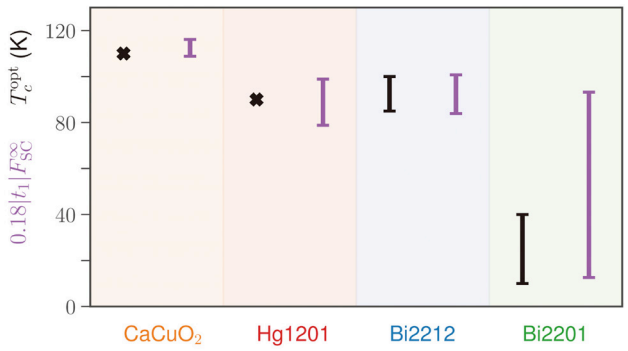

Fig. 1. Comparison of experimentally optimal critical temperature, T_c^{opt} (black symbols) and the scaling formula 0.16 $t_1 F_{SC}^{\infty}$ (purple symbols) obtained from the *ab initio* parameter t_1 (nearest neighbor electron transfer) and the calculated order parameter F_{SC}^{∞} [3]. Calculated results reproduce experimental trend of T_c quantitatively for carrier doped $CaCuO_2$, $HgBa_2CuO_4$ (Hg1201), $Bi_2Sr_2CaCu_2O_8$ (Bi2212), and $Bi_2Sr_2CuO_6$ (Bi2201) .

well accounts for spectroscopic data otherwise puzzling, by combining experimental and computational results with the help of machine learning in the analyses of angle resolved photoemission and the resonant inelastic X-ray scattering results [4-7].

Another challenge of condensed matter physics is the nature of quantum fluids, especially, the quantum spin liquid since the first proposal half a century ago [8]. It was shown with the aid of supercomputers that the quantum spin liquid phase indeed exists and the spin excitations are well described by the fractionalized spinons in gapless quantum spin liquids, where the spinon has the Dirac-type gapless excitation and an observable spin excitation is represented by the two composite excitations of the spinon [9,10]. *Ab initio* calculations of molecular solid called dmit salts indeed demonstrated that this picture holds and the experimental phase diagram of the dmit salts is reproduced [10] as shown in Fig. 2 and the quantum spin liquid established in a theoretical touchstone model, J_1-J_2 Heisenberg Hamiltonian on the square lattice also shows essentially the same structure of the fractionalized excitation [9]. These findings were made it possible by the progress in quantum many-body solver using the neural network [11].

The electron fractionalization found in the cuprate superconductors and the fractionalization of an electronic spin into two spinons look quite different at a glance. However, the

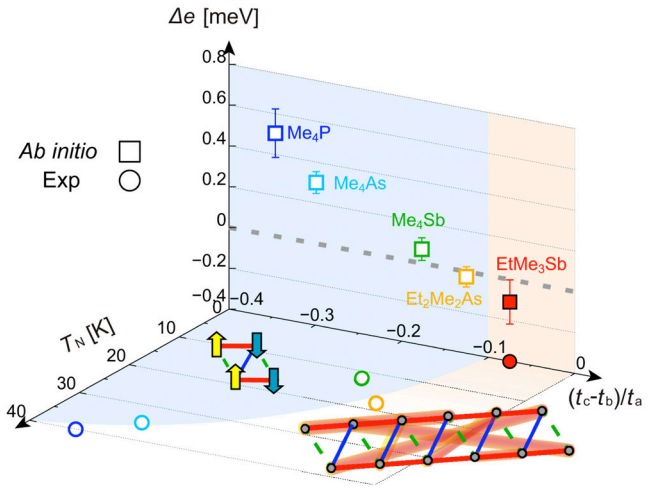

Fig. 2. Ground-state phase diagram revealed by *ab initio* simulations (vertical plane), which shows agreement with the experimental phase diagram (bottom plane) for molecular solid, dmit salts with five different cations [10].

essence of the superconducting state as well as the quantum spin liquid lies in the way of constructing quantum mechanically entangled state, the element of which is commonly the paired state of two electrons with further entanglement of the pairs. Indeed, the wavefunctions have a common structure of the pair-product functions at the core. The quantum entanglement by the spin singlet constituting the quantum spin liquid and by the exciton leading to the electron fractionalization are represented in the extended Hilbert space in a unified fashion and the singlet and exciton take on different aspect of the same entanglement [4].

Acknowledgements

This report is based on the collaborations with Michael Schmid, Jean-Baptiste Morèe, Youhei Yamaji, Motoaki Hirayama, Yusuke Nomura, Di-Jing Huang, Atsushi Fujimori, Teppei Yoshida, Kota Ido, Takahiro Misawa, and Kazuyoshi Yoshimi.

References

[1] M. Imada and T. Miyake, J. Phys. Soc. Jpn. **79,** 112001 (2010).
[2] J.-B. Morèe, M. Hirayama, M. T. Schmid, Y. Yamaji, and M. Imada, Phys. Rev. B **106**, 235150 (2022).
[3] M. T. Schmid, J.-B. Morèe, Y. Yamaji, and M. Imada, arXiv:2303.06672.
[4] M. Imada, J. Phys. Soc. Jpn. **90**, 111009 (2021).
[5] M. Imada, J. Phys. Soc. Jpn. **90**, 074702 (2021).
[6] A. Singh, H. Y. Huang, J. D. Xie, J. Okamoto, C. T. Chen, T. Watanabe, A. Fujimori, M. Imada, D. J. Huang, Nat. Commun. **13**, 7906 (2022).
[7] Y. Yamaji, T. Yoshida, A. Fujimori, M. Imada, Phys. Rev. Research **3**, 043099 (2021).
[8] P. Fazekas and P. W. Anderson, Phil. Mag. **30**, 423 (1974).
[9] Y. Nomura and M. Imada, Phys. Rev. X **11**, 031034 (2021).
[10] K. Ido, K. Yoshimi, T. Misawa, and M. Imada, npj Quantum Mater. **7**, 48 (2022).
[11] Y. Nomura, A. S. Darmawan, Y. Yamaji and M. Imada, Phys. Rev. B **96**, 205152 (2017).

Authors
M. Imada[a,b,c]
[a] Waseda University
[b]Sophia University
[c]Toyota Physical and Chemical Research Institute

PI of Joint-use project: M. Imada
Host lab: Supercomputer Center

Acceleration of First-Principles Statistical Thermodynamics Framework abICS Using an On-Lattice Neural Network Model and Active Learning

In 2019, ab Initio Configuration Sampling toolkit, or abICS for short, was developed as an ISSP Software Advancement Project for directly combining first-principles relaxation and total energy calculations with replica exchange Monte Carlo (RXMC) sampling [1]. The motivation was that effective models such as cluster expansion, which are used to speed up the usual Metropolis Monte Carlo sampling for analyzing order/disorder in alloy systems, are limited in describing complex many-component systems with sufficient accuracy. Our aim at that time was to enable direct sampling on first-principles energies by employing highly parallel sampling methods such as RXMC in combination with massively parallel supercomputing resources. A few years later, some of the authors found that an on-lattice neural network model overcomes many issues found in previous effective models if sufficient training data is provided in an active learning setting [2,3]. This led to the

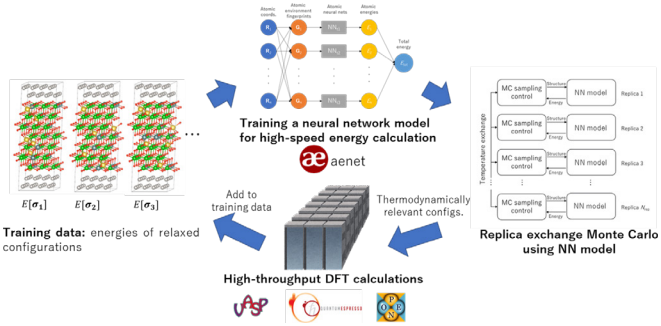

Fig. 1. Overview of the active learning procedure using abICS

proposal of last year's Software Advancement Project, which we outline in this report.

The abICS framework developed in this project uses Python as a glue language to piece together the necessary components (Fig. 1). It is registered on PyPI (Python Package Index; pypi.org) and can be installed easily in most environments through the command "`pip install --user abics`". A typical use case is outlined as follows:

1. Random configurations on a lattice are relaxed and their total energies are calculated using the first-principles code of choice. We support VASP, Quantum Espresso, and OpenMX.
2. A neural network model is trained on data from step 1 to predict relaxed energies from configurations on the non-relaxed lattice. We currently use aenet code [4] for the neural network training.
3. RXMC or population annealing MC (PAMC) calculation is performed using the neural network model from step 2. Two sampling modes are available: canonical sampling with a fixed number of atoms or grand canonical sampling which allows for changes in the composition. For the neural network evaluation, we provide a file IO-based interface to aenet, and we also provide an interface to aenet-lammps [5] python interface which does not rely on file IO and is thus usually faster.
4. A subset of samples from step 3 are relaxed and their total energies are calculated using first-principles calculation. If the results deviate considerably from the neural network prediction, the data is added to the training data set and the procedure is repeated from step 2.

The overall procedure is controlled by an input file in TOML format, which is an easy-to-read software configuration format that is being used in many projects [6]. The parameters for the first-principles calculations and neural network training/evaluation are controlled by separate files following formats of the specified solver.

We believe that abICS will be a game-changer in modeling order/disorder in many-component crystalline systems as we have already demonstrated for partially hydrated Sc-doped $BaZrO_3$ [3]. Please do not refrain from contacting us if you find any difficulties in using or extending this software.

References
[1] S. Kasamatsu and O. Sugino, J. Phys.: Condens. Matter **31**, 085901 (2019).
[2] S. Kasamatsu *et al*., J. Chem. Phys. **157**, 104114 (2022).
[3] K. Hoshino, S. Kasamatsu *et al*., Chem. Mater. **35**, 2289 (2023).
[4] N. Artrith *et al*., Phys. Rev. B **96**, 014112 (2017).
[5] M. S. Chen *et al*., J. Chem. Phys. **155**, 074801 (2021).
[6] https://github.com/toml-lang/toml

Authors
S. Kasamatsu[a], T. Aoyama, Y. Motoyama, K. Yoshimi, and O. Sugino
[a]Yamagata University

PI of Joint-use project: S. Kasamatsu
Host lab: Supercomputer Center

Topological Hall Effect Induced by Non-Coplanar Magnetic Structure in van der Waals Magnets

Antiferromagnets with broken time-reversal symmetry (TRS) have been attracting remarkable attention since the discovery of the large Hall effect in the kagome antiferromagnet Mn_3Sn [1], which exhibits a coplanar 120-degree spin order on the kagome lattice. From the viewpoint of symmetry, this magnetic structure is compatible with the in-plane ferromagnetic order, and thus accounts for the large Hall effect despite the extremely small net magnetization. These properties would be applicable for novel information storage/processing devices with small stray fields and faster spin dynamics. Thus far, the number of this class of materials has been limited, and further exploration of TRS-broken antiferromagnets is highly demanded.

In the present study, we focus on the van der Waals materials composed of triangular lattice layers of magnetic ions, $CoTa_3S_6$ (CTS) and $CoNb_3S_6$ (CNS), which have been recently reported to show large Hall effect in the antiferromagnetic ordered phases [2,3]. However, the magnetic structures of these compounds were not investigated in detail. We thus performed polarized neutron scattering experiments on these compounds at the POlarized Neutron Triple-Axis spectrometer (PONTA) installed in the 5G beamline of the Japan Research Rector 3 (JRR-3), in order to elucidate the magnetic structure relevant to the large Hall effect [4].

Single crystals of CTS and CNS were synthesized by the chemical vapor transport method. As for CTS, we observed the large spontaneous Hall effect in zero magnetic field, as shown in Fig. 1(a), as if the conduction electrons were subject to a magnetic field along the c axis of the crystal. We mounted a single crystal of CTS on a standard ^{4}He closed-cycle refrigerator with the (H,K,0) scattering plane, and measured magnetic reflections with polarized neutrons. Figures 2(a) and 2(b) show the scattering profiles of the magnetic Bragg peaks at (1/2,0,0) and (1/2,1/2,0) at the lowest temperature. The incident neutrons were polarized along the c axis of the crystal, that was perpendicular to the scattering plane. By using a spin flipper and an analyzer of a magnetic Heusler-alloy crystal, we measured the intensities of the scattered neutrons in the non-spin-flip (NSF) and spin-flip (SF) channels, which correspond to the Fourier-transformed magnetic moments parallel to the c axis and that perpendicular to both the c axis and the scattering vector, respectively. We found that the reflection at (1/2, 1/2, 0) contains both the NSF and SF signals, suggesting that the system has non-coplanar magnetic structure. By representation analysis, we obtained possible bases of the magnetic structure, and found that the observed SF and NSF intensities can be reproduced by the all-in-all-out type magnetic structure constructed by a linear combination of the possible bases, as shown in Figs. 2(c) and 2(d). This magnetic structure breaks the time-reversal symmetry, and thus has the two domains, each of which is interconverted to the other by the time-reversal operation. Therefore, these two domains are

compatible with the ferromagnetic state with up and down magnetic moments, respectively, and exhibit the large Hall effect with opposite signs. We also investigated the magnetic structure of CNS in the same manner, and found that this system also has the all-in-all-out type non-coplanar magnetic structure. We also performed time-of-flight neutron diffraction measurements on CTS in Material and Life-science experimental Facility (MLF) of J-PARC, and also carried out first-principles calculations based on the density functional theory. Both confirmed the all-in-all-out magnetic structure. We note here that this magnetic structure has finite scalar spin chirality, $S_i \cdot (S_j \times S_k)$, which can induce a fictitious magnetic field acting only on the conduction electrons by adding quantum-mechanical Berry phase to their wavefunctions. The present results indicate that the scalar spin chirality mechanism can offer a promising route to realize giant spontaneous Hall response even in compensated antiferromagnets.

References

[1] S. Nakatsuji *et al*., Nature **527**, 215 (2015).
[2] N. J. Ghimire *et al*., Nature Commun. **9**, 3280 (2018).
[3] P. Park *et al*., npg Quantum Materials **7**, 42 (2022).
[4] H. Takagi *et al*., Nature Physics (advanced online publication) (2023).

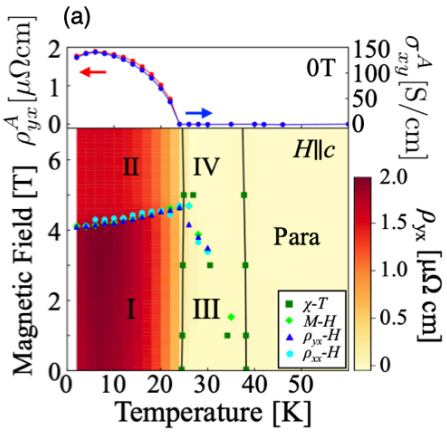

Fig. 1. (upper panel) Temperature dependence of the Hall resistivity and conductivity of CTS measured in zero field. (lower panel) Color map of thethe Hall resistivity superposed on the magnetization-temperature phase diagram of CTS.

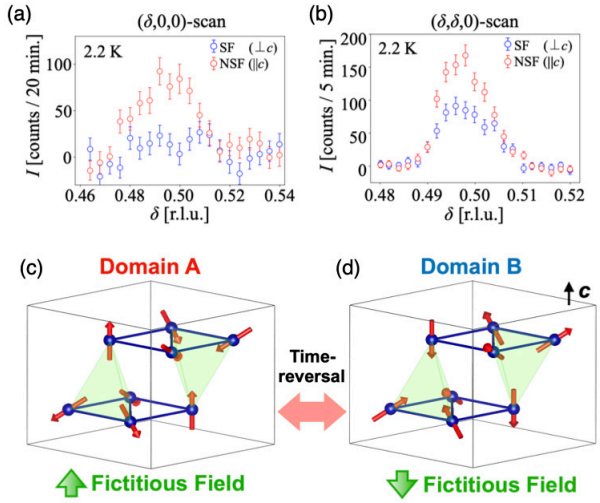

Fig. 2. [(a),(b)] Polarized neutron scattering profiles of CTS. [(c),(d)] Two domains of all-in-all-out magnetic structure.

Authors
H. Takagi[a], R. Takagi[a,b,c], S. Minami[a], T. Nomoto[a], K. Ohishi[d], M.-T. Suzuki[e,f], Y. Yanagi[e,g], M. Hirayama[a,c], N. D. Khanh[c], K. Karube[c], H. Saito[a], D. Hashizume[c], R. Kiyanagi[h], Y. Tokura[a,c], R. Arita[a,c], T. Nakajima[a,c], and S. Seki[a,b,c]
[a]The university of Tokyo
[b]PRESTO, Japan Science and Technology Agency (JST)
[c]RIKEN Center for Emergent Matter Science (CEMS)
[d]Comprehensive Research Organization for Science and Society (CROSS)
[e]Tohoku University
[f]Osaka University
[g]Toyama Prefectural University
[h]J-PARC Center

PI of Joint-use project: S. Seki
Host lab: Neutron Science Laboratory

Large Anomalous Hall Effect Induced by Field-Tunable Weyl Points in Antiferromagnetic Degenerate Semiconductor $EuMg_2Bi_2$

Weyl magnets, which have the topologically nontrivial band crossing points, have recently attracted significant attention because of the unconventional physical properties, such as large anomalous Hall effects (AHE). The typical materials have a semimetallic band structure where many bands cross the Fermi energy (E_F), resulting in complicated band structures and Fermi surfaces that hinder a simple understanding of their Weyl physics. In this study, we report on the field-tunable Weyl points in the degenerate antiferromagnetic semiconductor $EuMg_2Bi_2$, which has a simple and small Fermi surface. $EuMg_2Bi_2$ has a $CaAl_2Si_2$-type structure, which consists of the alternative stacking of the Eu magnetic layer and the Mg_2Bi_2 buckled-honeycomb layer (Fig. 1(a)). The former layer exhibits the A-type antiferromagnetic (A-AFM) order below $T_N \sim 6.7$ K at zero field. When the field is applied along the c -axis, Eu spins start canting toward the c-axis and are fully polarized above $B_c \sim 4$ T at 2 K. The latter layer forms the semiconducting band with the direct band gap at the Γ point, resulting in the simple Fermi surface. Therefore, it is expected that, in the magnetic field, the spin-polarized band crossing points (Weyl points) are formed while maintaining a simple band structure due to the spin splitting caused by the exchange interaction with local Eu spins. To reveal the impacts of the Eu magnetism on the band structure of $EuMg_2Bi_2$, we synthesized the large single crystal (Fig. 1(b)) and performed the various measurements and the first-principles calculations.

Figure 1(c) shows the field dependence of the Hall resistivity ρ_{yx} at 2 K for the field along the c-axis. Although, ρ_{yx} is almost linear with respect to field above B_c, it deviates from the straight line below B_c and shows a hump structure at approximately 2.5 T. This signals the AHE coupled with Eu magnetic order. To extract the anomalous component ρ^A_{yx} , we estimate the ordinary component $\rho^N_{yx} = R_H B$ from the data above B_c. We obtained the anomalous component as $\rho^A_{yx} = \rho_{yx} - \rho^N_{yx}$ which is roughly proportional to magnetization. At $B > B_c$, the anomalous Hall angle $\Theta_{AH} = \sigma^A_{xy}/\sigma_{xx}$, where $\sigma^A_{xy} = \rho^A_{yx}/(\rho^2_{xx} + \rho^2_{yx})$ and $\sigma_{xx} = \rho_{xx}/(\rho^2_{xx} + \rho^2_{yx})$ exhibits the nearly constant value (~ 0.07), which is comparable to those reported for other Weyl ferromagnets $Co_3Sn_2S_2$ (~ 0.2 at 150 K) [2], Fe_3GeTe_2 (~ 0.09 at 2 K) [3], and GdPtBi (~ 0.15 at 2.5 K) [4]. Such a large Θ_{AH} indicates that $EuMg_2Bi_2$ has band crossing points near E_F in the forced-ferromagnetic (f-FM) phase as a source of the Berry

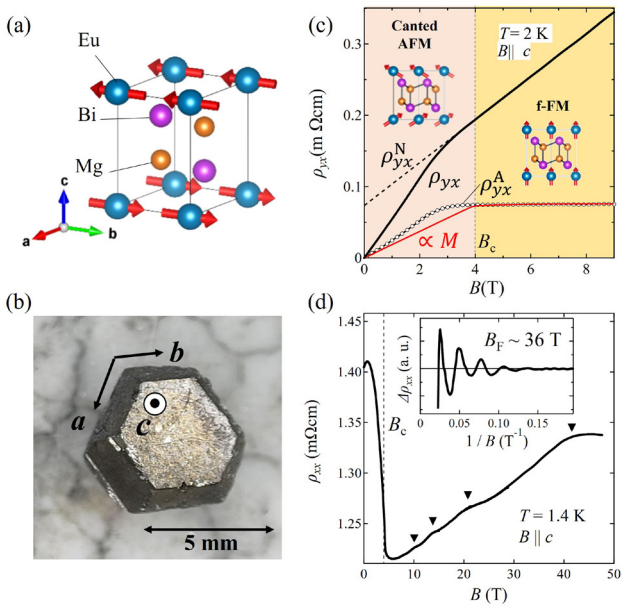

Fig. 1. (a) The crystal structure of $EuMg_2Bi_2$. (b) The photograph of the single crystal of $EuMg_2Bi_2$. (c) The field dependence of ρ_{yx} and its anomalous part ρ_{yx}^A at 2 K. The black dotted line corresponds to the ordinary part ρ_{yx}^N obtained from the liner fit to the experimental data above B_c. Note here that the ρ_{yx}^N is vertically shifted to demonstrate the fitted result at the high-field region. The red curve represents the field dependence of the magnetization M at 2 K. Insets show the magnetic structure of Eu spins at canted-antiferromagnetic (AFM) and forced-ferromagnetic (f-FM) phases. (d) Field dependence of ρ_{xx} at T = 1.4 K up to B ~ 50 T. Triangles denote the oscillatory component. The inset shows the oscillatory component $\Delta\rho_{xx}$.

curvature.

To obtain the detailed information of the Fermi surface, we measured the several physical properties up to ~ 55 T using the nondestructive mid-pulse magnet. Figure 1(d) shows the field dependence of the resistivity ρ_{xx}. As denoted by black triangles, we observed clear oscillatory structure. These oscillations are periodic with respect to $1/B$ [see inset of Fig. 1(d)], which indicates the quantum oscillation arising from the Landau quantization. By Onsager's theorem, we can estimate the cross-section S_F (~ 0.352 nm^{-2}) of the Fermi surface from the oscillation frequency B_F (~ 36 T), which allows us to determine the position of E_F in combination with the first-principles calculation shown below.

Figure 2(a) shows the calculated band structure around the Γ point for A-AFM phase. The two valence bands I and II cross each other on the Γ−A line, leading to a Dirac-like point located far from the E_F. When the field is applied along the c-axis, both bands exhibit a spin splitting because of the exchange interaction with the local Eu spins to form the multiple Weyl points. The position of the Weyl points shifts with increasing the magnitude of the spin splitting. Intriguingly, in the f-FM phase, one of the Weyl points are formed in the vicinity of E_F (Fig. 2(b)), which is determined to be ~ 110 meV from the comparison between the experimental and theoretical values of S_F and carrier density obtained from the Hall coefficient [1]. To clarify the intrinsic AHE due to the Berry curvature of the Weyl point, we calculated the E_F dependence of the anomalous Hall conductivity σ_{xy}^A in the f-FM phase. The calculated σ_{xy}^A shows a peak near the experimental E_F value where the Weyl point exists, and a good quantitative agreement with the experimental result obtained by the carrier-tuned samples. This strongly indicates that the observed large AHE in $EuMg_2Bi_2$ is due to the Berry curvature at the Weyl point induced by the magnetic field.

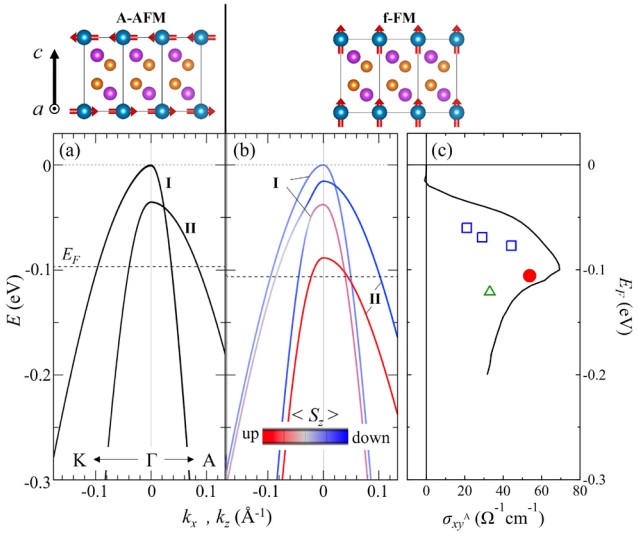

Fig. 2. (a, b) Valence band structures around the Γ point near E_F (lower panels) for various magnetic states (upper panels). Red and blue colors of band dispersions represent spin up and spin down, respectively. The dotted lines denote the Fermi energy E_F determined from the quantum oscillation frequency B_F at T = 1.4 K. (c) Anomalous Hall conductivity σ_{xy}^A as a function of E_F. The solid black curve represents the calculated result for the f-FM phase. The solid red circle denotes the experimental data (2 K, 9 T) for pristine $EuMg_2Bi_2$, while the open blue squares and open green triangle denote those for the annealed crystals and In-doped crystal, respectively.

Thus, our findings have clarified the unambiguous relationship between the emergent Weyl points and the anomalous Hall effect in a simple band structure, providing a guiding principle for future material design.

References

[1] M. Kondo *et al*., Physical Review B **107**, L121112 (2023).
[2] E. Liu *et al*., Nat. Phys. **14**, 1125 (2018).
[3] K. Kim *et al*., Nat. Mater. **17**, 794 (2018).
[4] T. Suzuki *et al*., Nat. Phys. **12**, 1119 (2016).

Authors

M. Kondo[a], M. Ochi[a], R. Kurihara[b], A. Miyake, Y. Yamasaki[c, d], M. Tokunaga, H. Nakao[e], K. Kuroki[a], T. Kida[f], M. Hagiwara[f], H. Murakawa[a], N. Hanasaki[a], and H. Sakai[a]

[a]Osaka University
[b]Tokyo University of Science
[c]NIMS
[d]CEMS, RIKEN
[e]KEK
[f]AHMF, Osaka University

PI of Joint-use project: H. Sakai
Host lab: Tokunaga Group

High Upper Critical Field of 120 T and Small Anisotropy in Highly Hydrogen-Substituted SmFeAsO Epitaxial Film

Among iron-based bulk superconductors, the highest critical temperature (T_c) of 55 K has been recorded for the 1111-type SmFeAsO. The superconductivity emerges by electron doping through partial substitution of F^- or H^- in the O^{2-} sites. Recently, we succeeded in fabrication of H-substituted SmFeAsO epitaxial thin films using topochemical reaction with binary dihydrides. The H-substituted SmFeAsO films exhibit not only high T_c, but also high critical current density (J_c), which is comparable with those of high J_c films of 122-type $BaFe_2As_2$ that is regarded as the most promising candidate among iron-based superconduc-

tors for practical application. Other than T_c and J_c, the upper critical field ($\mu_0 H_{c2}$) and its anisotropic parameter ($\gamma \equiv H_{c2\parallel}/H_{c2\perp}$, where the directions of the applied external magnetic fields are parallel ($\mu_0 H \parallel$) and perpendicular ($\mu_0 H \perp$) to the *ab* plane of SmFeAsO.) are also the important properties for evaluation of superconductors and their applications. In this study, the electronic transport properties of the highly H-substituted SmFeAsO epitaxial film were investigated to determine the low-temperature and high-field limits of its $\mu_0 H_{c2}$ ($\mu_0 H_{c2}(0)$) and γ under extremely high magnetic fields generated by nondestructive (60 T) and single-turn (130 T) pulsed magnets at the ISSP.

To experimentally determine $\mu_0 H_{c2}(0)$ for $\mu_0 H \parallel ab$, we performed radio-frequency (rf) impedance measurement with the single-turn magnet up to 130 T at 2.2 K (Fig. 1). The sample resistance (R) was roughly proportional to the inverse ratio of the amplitude of the reflection rf signal to the incident rf excitation with a field-independent background (Γ^{-1}). Even though Γ^{-1} remained constant with the wire resistance due to two-wire configuration between 0 and ~100 T, Γ^{-1} steeply increased at higher fields. An enlarged view of the high-field region in Fig. 1(a) is shown in Fig. 1(b). From the least-squares fits, clear saturation of Γ^{-1} was observed above ~125 T. By taking $\mu_0 H$ where Γ^{-1} became 80% of the saturated Γ^{-1} as $\mu_0 H_{c2}$, $\mu_0 H_{c2}$ of H-substituted SmFeAsO at 2.2 K was estimated to be 120 T for $\mu_0 H \parallel ab$. Because the experimentally confirmed $\mu_0 H_{c2}$ at 2.2 K should be almost the same as its low-temperature limit $\mu_0 H_{c2}(0)$, we concluded that $\mu_0 H_{c2}(0)$ of H-substituted SmFeAsO film reaches 120 T. This is the first experimental determination of $\mu_0 H_{c2}$ for 1111-type SmFeAsO at the low-temperature and high-field limits, and it is the highest value among those of other iron-based superconductors.

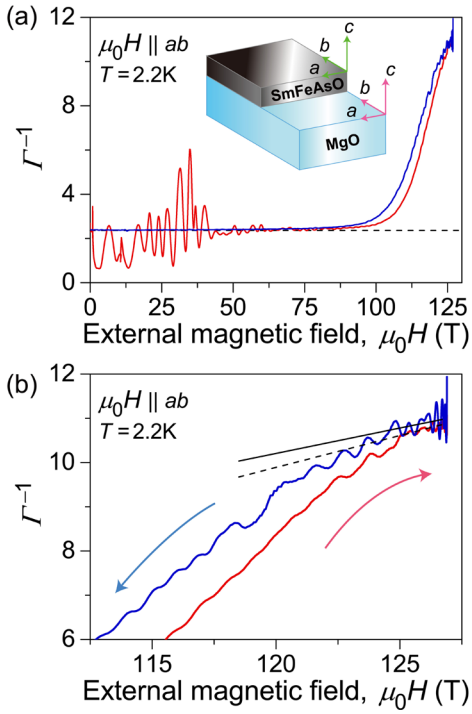

Fig. 1. Impedance measurement under high magnetic fields of up to 130 T at 2.2 K. The magnetic field was generated by the single-turn magnet and applied within the *ab* plane. (a) Γ^{-1} in the field region from 0 to 130 T. The inset shows relationship between the crystallographic orientation and the sample configuration of the H-substituted SmFeAsO epitaxial film on a MgO single-crystal substrate. (b) Enlarged image of (a) in the high-field region. The constant background is indicated by a black dashed line in (a). The red and blue arrows in (b) denote the directions of the field sweep. The black dashed and solid lines in (b) are the least-squares fits of the normal-state resistance in the up and down sweeps.

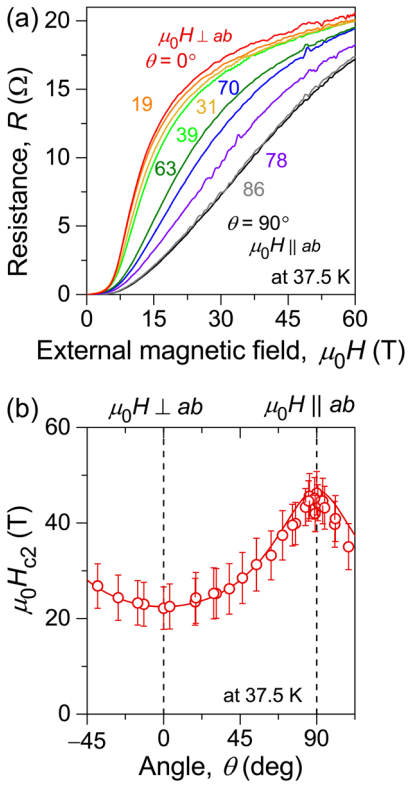

Anisotropic parameter of $\mu_0 H_{c2}$ (γ) in the H-substituted SmFeAsO epitaxial film. (a) R–$\mu_0 H$ curves under $\mu_0 H$ of up to 60 T at 37.5 K as a function of the angle (θ). (b) Angular dependence of $\mu_0 H_{c2}$ at 37.5 K. The red curve is the fit obtained by two-band analysis.

Next, to determine γ, the H-substituted SmFeAsO epitaxial film was mounted on a rotator probe, where the angle between the field direction and the *c* axis of the film was defined as θ, and $\mu_0 H$ was applied with the nondestructive pulsed magnet up to 60 T. Figure 2(a) shows the R–$\mu_0 H$ curves at 37.5 K with different field angles θ. With increasing θ, the jump in the R–$\mu_0 H$ curve gradually shifted to the higher field side. This experiment revealed that although there is a non-negligible angle dependence in $\mu_0 H_{c2}$, γ seems to be very small despite the layered structure of H-substituted SmFeAsO, which consists of individual SmO insulating and FeAs conductive layers. The θ dependence of $\mu_0 H_{c2}$ was estimated from the θ-dependent R (Fig. 2(b)), revealing that the γ around T_c is ~2. This small γ is comparable with those of MgB_2 and 122-type $BaFe_2As_2$, and almost half of that of F-substituted SmFeAsO ($\gamma > 4$). The small γ value of H-substituted SmFeAsO mainly originates from realization of three-dimensional superconductivity owing to high H incorporation.

In summary, we clarified the remarkable and unique characteristics in the H-substituted SmFeAsO epitaxial film such as the high $\mu_0 H_{c2}(0)$ of 120 T and relatively isotropic γ (~2) under extremely high magnetic fields generated by nondestructive and single-turn pulsed magnets at the ISSP [1]. Owing to the high and nearly isotropic $\mu_0 H_{c2}$, as well as the high T_c and high J_c, H-substituted SmFeAsO is a promising candidate for superconducting applications, such as the wires and tapes for cables and high-field electromagnets.

Reference

[1] K. Hanzawa, J. Matsumoto, S. Iimura, Y. Kohama, H. Hiramatsu, and H. Hosono, Phys. Rev. Mater. **6**, L111801 (2022).

Authors
K. Hanzawa[a], J. Matsumoto[a], S. Iimura[a, b], Y. Kohama, H. Hiramatsu[a], and H. Hosono[a, b]
[a]Tokyo Institute of Technology
[b]NIMS

PI of Joint-use project: H. Hiramatsu
Host lab: Kohama Group

Time-Resolved Angle-Resolved Photoemission Spectroscopy on $Ta_2Ni_{0.9}Co_{0.1}Se_5$

Ultrafast optical response of $Ta_2Ni_{0.9}Co_{0.1}Se_5$ has been studied by means of time-resolved angle-resolved photoemission spectroscopy (tr-ARPES). The Ti:Sapphire laser pulse with hν = 1.55 eV was used for the pump light and its higher harmonics with hν = 21.7 eV was employed for the probe light. The temporal resolution of the tr-ARPES is about 80 fs. $Ta_2Ni_{0.9}Co_{0.1}Se_5$ has a quasi one-dimensional crystal structure (Ta chain and Ni chain run along the a axis) and is one of the excitonic insulator (EI) candidates where the transition temperature is reduced by Co substitution in Ta_2NiSe_5. Under the sufficient incident fluence (1.9 mJ cm^{-2}), the conduction band is clearly observed above the Fermi level and the energy gap between the conduction and valence bands is closed at the delay time about 150 fs [1]. This observation suggests a photoinduced phase transition from the EI state to a semimetal state. The observed band dispersions of the semimetal phase roughly agree with the generalized gradient approximation (GGA) calculation which fails to reproduce the band gap at the ambient condition.

In Fig. 1, the tr-ARPES spectra of the semimetal phase are differentiated two times with respective to energy and are smoothed [2]. In this measurement, the Fermi surfaces are observed even before the arrival of the pump pulse (-400 fs). k_x represents a momentum along the Ta/Ni chain direction along which the valence and the conduction bands exhibit large dispersions. The k_x dispersions appreciably depend on k_y which is a momentum perpendicular to the Ta/Ni chains. The crosses indicate the band positions extracted from the momentum distribution curves (MDCs). The agreement between the band positions and the band structure calculations is not perfect, but the positions of the valence and conduction bands are roughly reproduced. Most probably, the electron-hole interaction, which is not exactly included in GGA, is screened out by the photoexcited carriers. In the photoinduced semimetal phase, the conduction and valence bands provide quasi one-dimensional Fermi surfaces with similar momentum positions suggesting a quasi one-dimensional line-node semimetal.

In most of the tr-ARPES measurements, the EI gap of $Ta_2Ni_{0.9}Co_{0.1}Se_5$ remains before the pump pulse arrival and is gradually suppressed after the pump pulse excitation. Such spectral behavior is clearly demonstrated in Fig. 2, where the energy distribution curves (EDCs) are numerically deconvoluted and divided by Fermi-Dirac distribution functions in order to extract the intrinsic spectral function [3]. With the fluence of 3.00 mJcm^{-2} and at the delay time of 70 fs, the valence band top does not reach the Fermi level creating a partial gap or a pseudogap, and the transition from the EI state to the semimetal state is not completed. While the conduction band crossing the Fermi level is observed with the shorter delay time (down to 50-70 fs) and/or the

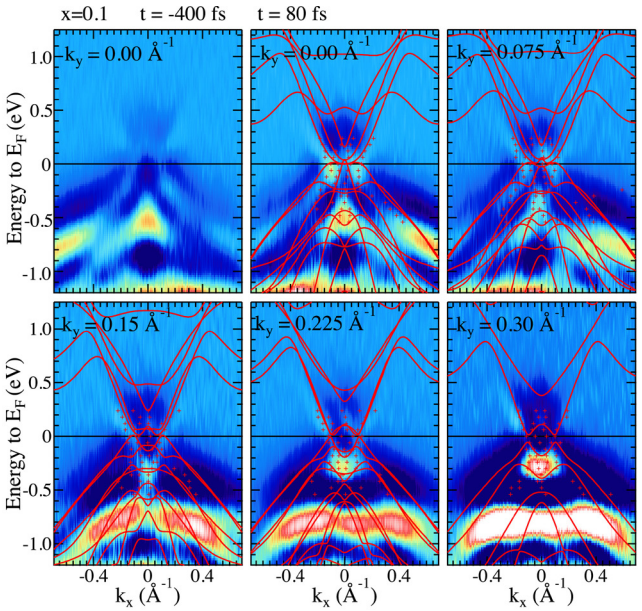

Fig. 1. The second derivatives of the tr-ARPES spectra with respective to energy as functions of k_x for $Ta_2Ni_{0.9}Co_{0.1}Se_5$, which are taken at 100 K with pump-probe delay of -400 fs (only k_y = 0.00 Å^{-1}) and about 100 fs (k_y = 0.00, 0.075, 0.15, 0.225, and 0.30 Å^{-1}). The symbols indicate the band positions extracted from MDCs. The solid curves indicate calculated GGA band dispersions for Ta_2NiSe_5.

lower fluence (down to 0.32 mJ cm^{-2}), the valence band top stays well below the Fermi level up to the fluence of 1.39 mJ cm^{-2} even at the delay time of 150-170 fs. Only with the highest fluence (3.00 mJ cm^{-2}) and the delay time of 150-170 fs, the gap (or pseudogap) at the Fermi level is closed. Such different optical responses of the valence and conduction bands cannot be explained by the canonical EI scenario, suggesting a vital role of electron-lattice coupling. One can speculate that the fluctuations of the Ni-Se bond, which can be coupled to the negative charge-transfer energy state ($d^9\underline{L}$ state) of Ni ($\underline{L}$ represents a Se 4p hole), remain at the 50-70 fs delay time and suppress the valence band shift. Around the delay time of 150-170 fs, the lattice fluctuations

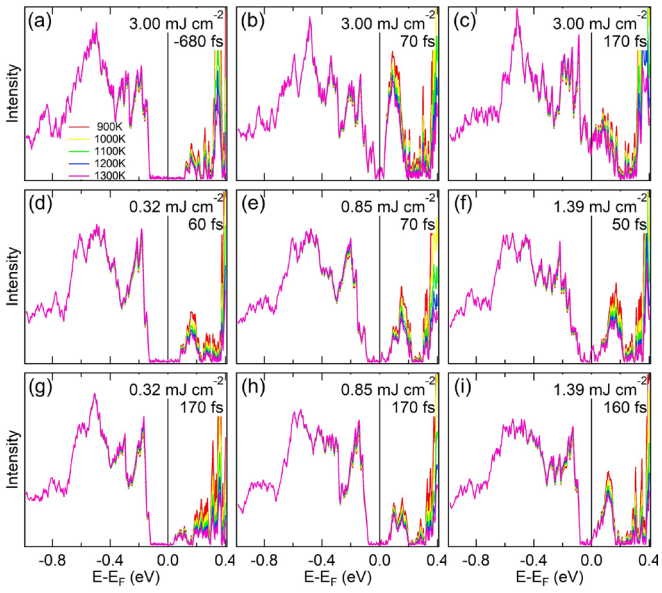

Fig. 2. EDCs (integrated in the k_x range between 0.05 and -0.05 Å^{-1}) deconvoluted and divided by the Fermi-Dirac distribution functions at the delay time of (a) -680 fs, (b) 70 fs, and (c) 170 fs for the fluence of 3.00 mJ cm^{-2}. Deconvoluted EDCs at 50-70 fs for the fluence of (d) 0.32 mJ cm^{-2}, (e) 0.85 mJ cm^{-2}, and (f) 1.39 mJ cm^{-2}. Deconvoluted EDCs at 150-170 fs for the fluence of (g) 0.32 mJ cm^{-2}, (h) 0.85 mJ cm^{-2}, and (i) 1.39 mJ cm^{-2}.

are screened out due to the photoexcited holes resulting in the semimetal phase with the substantial energy overlap between the conduction and valence bands. Such electron-lattice coupling is expected to be weak for the Ta-Se bond where the extended Ta 5d orbitals form the conduction band.

References
[1] T. Mitsuoka, T. Suzuki, H. Takagi, N. Katayama, H. Sawa, M. Nohara, M. Watanabe, J. Xu, Q. Ren, M. Fujisawa, T. Kanai, J. Itatani, S. Shin, K. Okazaki, and T. Mizokawa, J. Phys. Soc. Jpn. **89**, 124703 (2020).
[2] T. Mitsuoka, Y. Takahashi, T. Suzuki, M. Okawa, H. Takagi, N. Katayama, H. Sawa, M. Nohara, M. Watanabe, J. Xu, Q. Ren, M. Fujisawa, T. Kanai, J. Itatani, K. Okazaki, S. Shin, and T. Mizokawa, J. Phys. Soc. Jpn. **92**, 023703 (2023).
[3] Y. Takahashi, T. Suzuki, M. Hattori, M. Okawa, H. Takagi, N. Katayama, H. Sawa, M. Nohara, Y. Zhong, K. Liu, T. Kanai, J. Itatani, S. Shin, K. Okazaki, and T. Mizokawa, J. Phys. Soc. Jpn. in press.

Authors
T. Mizokawa[a], T. Mitsuoka[a], Y. Takahashi[a], M. Hattori[a], M. Okawa[a], T. Suzuki, and K. Okazaki
[a]Waseda University

PI of Joint-use project: T. Mizokawa
Host lab: Okazaki Group